Boxing-in of a blender in a Hénon-like family

Stefanie Hittmeyer, Bernd Krauskopf, Hinke M. Osinga
Department of Mathematics, The University of Auckland, Auckland 1142, New Zealand

Katsutoshi Shinohara
Graduate School of Commerce and Management, Hitotsubashi University, 2-1 Naka, Kunitachi, Tokyo 186-8601, Japan

November 2022

Abstract

The extension of the Smale horseshoe construction for diffeomorphisms in the plane to those in spaces of at least dimension three may result in a hyperbolic invariant set referred to as a blender. The defining property of a blender is that it has a stable or unstable invariant manifold that appears to have a dimension larger than expected. We consider here a Hénon-like family in $\mathbb{R}^3$, which features a blender in a certain range of a parameter (corresponding to an expansion or contraction rate). We consider the one-dimensional stable or unstable manifolds of a pair of saddle fixed points: the hyperbolic set containing these saddle points is a blender when the closure of these manifolds, seen from an appropriate direction, cannot be avoided by one-dimensional curves. This property has been used to detect numerically over which parameter range a blender exists in the Hénon-like family. We take here the complimentary approach of constructing an actual three-dimensional box (a parallelepiped) that acts as an outer cover of the hyperbolic set. The successive forward or backward images of this box form a nested sequence of sub-boxes that contains the hyperbolic set and its respective local invariant manifold. This constitutes a three-dimensional horseshoe that, in contrast to the idealised affine construction, is quite general and features sub-boxes with curved edges. The initial box is defined in a parameter-dependent way, and this allows us to characterise the hyperbolic set further in an intuitive way. In particular, tracing relevant edges of sub-boxes as a function of the parameter provides additional geometric insight into when the hyperbolic set may or may not be a blender.

1 Introduction

We construct a three-dimensional horsehoe for the Hénon-like family of diffeomorphisms

$$H(x, y, z) = (y,\, \mu + y^2 + \beta x,\, \xi z + y), \tag{1}$$

which was introduced and studied in [11, 12]; see also [6] for a Hénon-like endomorphism that motivated it. We will introduce the necessary theoretical concepts with specific reference to the family H in (1), whose phase space $\mathbb{R}^3$ has the lowest required dimension. In order to do so, we begin with some basic properties. The map H has skew-product structure: its restriction to the (x, y)-plane does not depend on z and is the Hénon map [10], written here in the form

$$h(x, y) = (y,\, \mu + y^2 + \beta x). \tag{2}$$

The z-coordinate of (1) implements a shear with contraction factor ξ, which we take to be positive throughout.

We fix $\mu = -9.5$ and $\beta = 0.3$, which ensures that the planar Hénon map h features a full Smale horseshoe; hence, h has a hyperbolic set Λ_h in the form of a Cantor set that is

topologically equivalent to a full shift on two symbols. This hyperbolic set arises as the closure of the intersection set of the stable and unstable manifolds of two saddle fixed points

$$p_h^{\pm} := \left(\rho^{\pm}, \rho^{\pm}\right),$$

where

$$\rho^{\pm} := \frac{1}{2}\left(1 - \beta \pm \sqrt{(1-\beta)^2 - 4\mu}\right).$$

For our choice of $\mu = -9.5$ and $\beta = 0.3$, the saddle points are at

$$p_h^- \approx (-2.7520, -2.7520) \quad \text{and} \quad p_h^+ \approx (3.4520, 3.4520).$$

The stable and unstable manifolds $W^s(\Lambda_h)$ and $W^u(\Lambda_h)$ of Λ_h are given as the closures of the manifolds $W^s(p_h^{\pm})$ and $W^u(p_h^{\pm})$, respectively. In particular, this means that $\Lambda_h = \overline{W^s(p_h^{\pm}) \cap W^u(p_h^{\pm})}$.

Due to the skew-product structure of (1), the hyperbolic set Λ_h of h lifts to a hyperbolic set Λ of H with similar properties. Namely, Λ is the closure of the intersection set of the stable and unstable manifolds $W^s(p^{\pm})$ and $W^u(p^{\pm})$ of two corresponding saddle fixed points

$$p^{\pm} := \left(\rho^{\pm}, \rho^{\pm}, \frac{\rho^{\pm}}{1-\xi}\right) \tag{3}$$

of H; furthermore, $W^s(\Lambda) = \overline{W^s(p^{\pm})}$ and $W^u(\Lambda) = \overline{W^u(p^{\pm})}$. The dimensions of these manifolds depend on the contraction factor $\xi \neq 1$, and we consider here the following two cases.

(1) $\xi > 1$, when there is expansion in the z-direction of H, which means that $\dim(W^s(p^{\pm})) = 1$ and $\dim(W^u(p^{\pm})) = 2$; and

(2) $0 < \xi < 1$, when there is contraction in the z-direction of H, which means that $\dim(W^s(p^{\pm})) = 2$ and $\dim(W^u(p^{\pm})) = 1$.

Owing to the skew-product nature of (1), for any ξ, the orthogonal projections of the global manifolds $W^s(p^{\pm})$ and $W^u(p^{\pm})$ of H onto the (x, y)-plane are the global manifolds $W^s(p_h^{\pm})$ and $W^u(p_h^{\pm})$ of the Hénon map h. In particular, the respective two-dimensional global manifolds, $W^u(p^{\pm})$ for $\xi > 1$ and $W^s(p^{\pm})$ for $0 < \xi < 1$, are the direct products of $\mathbb{R}$ (the z-direction) with $W^u(p_h^{\pm})$ and $W^s(p_h^{\pm})$, respectively.

In either case, for ξ sufficiently close to 1 the (transitive) hyperbolic set Λ is a *blender* [11, 12]. The concept of a blender was introduced by Bonatti and Díaz [2] to show that heterodimensional cycles and associated complicated dynamics may occur C^1-robustly in (non-uniformly hyperbolic) systems; see also [6, 2, 1, 4, 5, 3]. As in [11, 12], we use the definition of a blender from [6, 5] that says, colloquially speaking, that Λ is a blender if its one-dimensional global manifold — $W^s(\Lambda)$ for $\xi > 1$ and $W^u(\Lambda)$ for $0 < \xi < 1$ — acts geometrically as a set of dimension two. In more technical terms, the requirement is that there exists a C^1-open set of curve segments in the three-dimensional phase space that each intersect the respective one-dimensional manifold locally near Λ. Moreover, this property must be robust, that is, hold for the corresponding hyperbolic set of every sufficiently C^1-close diffeomorphism. In other words, seen from an appropriate direction the one-dimensional set $W^s(\Lambda)$ or $W^u(\Lambda)$, respectively, looks like a surface — in spite of the fact that it is a Cantor set of curves when viewed along the z-direction.

We refer to this defining characteristic of a blender as the *carpet property* [11, 12]. Since the one-dimensional global manifolds $W^s(p^{\pm})$ and $W^u(p^{\pm})$ of the fixed points $p^{\pm}$ are dense in $W^s(\Lambda)$ or $W^u(\Lambda)$, respectively, the carpet property can be verified numerically for the family H by checking whether these one-dimensional global manifolds fill out an area in projection. This is achieved by considering the intersection points of $W^s(p^{\pm})$ or $W^u(p^{\pm})$ with a plane and showing, for a suitable projection, that the (largest) gaps between them converge to 0 as the

arclength of the respective one-dimensional manifolds goes to infinity. The required very long one-dimensional global manifolds are computed as arclength-parametrised curves [15] after the phase space $\mathbb{R}^3$ has been compactified to $\mathcal{C} = \overline{\mathbb{D}} \times [-1, 1]$; see [11, 12] for details. In this way, we showed over which range near $\xi = 1$ the hyperbolic set Λ of H is indeed a blender. We also explored numerically how the carpet property is lost when ξ deviates too far from 1 and found that this happens via the creation of infinitely many robust gaps as ξ is varied.

In this paper, we focus on the complementary and arguably 'classical' perspective that the hyperbolic set Λ and its respective local one-dimensional manifold can be viewed geometrically as the invariant set of a three-dimensional horseshoe construction. By this we mean that a three-dimensional 'box' is stretched and folded under the given diffeomorphism in such a way that it intersects the box in two 'sub-boxes'. Indeed, the question "What is ... a blender?" is answered in [1] with an affine horsehoe construction, and the type of blender we find for the family H is also referred to as a blender-horseshoe [7, 8]. Indeed, in complete analogy with Smale's horseshoe construction, the illustrations in [1] and in [8] show how a box in phase space should map back to itself such that a blender is created in the limit of repeating this process.

The affine blender-horseshoe construction in [1] is idealised in that the abstract map consists locally of linear scalings that align with the respective coordinate axes; hence, the initial box and all of its iterates are cuboids. These properties are special, yet the affine construction still give insight into the geometry of a blender when the central contraction or expansion rate is near 1. On the other hand, the affine construction is not sufficiently representative for how a box maps in an actual example. In this paper we investigate what a more typical situation actually looks like. Apart from being of general interest, the nonlinear nature of the three-dimensional horseshoe turns out to be especially relevant when one is interested in the (dis)appearance of a blender as parameters change.

More specifically, for the Hénon-like family (1) we construct a parameter-dependent box — in the form of a parallelepiped — that is 'tight', meaning that the two sub-boxes that are its (pre)images extend to the boundary of the initial box. In contrast to the affine construction, these and further (pre)images under H are sub-boxes all have curved edges, so that neither their 'side' nor their 'front' faces line up exactly with the initial box. These additional properties represent a more realistic case of a three-dimensional horseshoe, and they provide a more intuitive idea of how the respective one-dimensional manifolds behave when the parameter ξ is varied. This will be illustrated in different ways: we present images that show (i) the initial box, its sub-boxes and the relevant global manifolds inside the box in the three-dimensional phase space of H; and (ii) their intersection sets with a suitably chosen plane. We provide such illustrations for the two cases that the hyperbolic set Λ is a blender and that it is not, both for $\xi > 1$ and for $0 < \xi < 1$. This allows us to identify which edges are responsible for the opening and closing of gaps in a certain projection as the carpet property of the respective one-dimensional manifold is lost. This geometric insight is then used to trace out the location of these edges in the parameter ξ, which provides an outer approximation of the ξ-range over which a blender may exist. These results show that the non-affine nature of the box construction indeed matters, especially when one is interested in how the carpet property is lost and the hyperbolic set ceases to be a blender. More generally, we believe that knowledge of the nonlinear nature of the three-dimensional horseshoe will be important if one wants to 'continue' a blender in parameters and/or construct a computer-assisted proof of its existence by means of verifying topological properties; for example, based on methods in [19, 18, 13].

The paper is organised as follows. In Sec. 2 we construct a box $\mathcal{B}$ for $\xi > 1$ that contains $W^s(\Lambda)$ in its sucessive preimages; we consider the properties of these preimages of $\mathcal{B}$ for the two cases $\xi = 1.2$ when Λ is a blender and for $\xi = 2.4$ when it is not. Similarly, Sec. 3 presents and shows a box $\mathcal{D}$ for $0 < \xi < 1$ and its images under H, which contain $W^u(\Lambda)$; again we show their properties when Λ is a blender and when it is not, for $\xi = 0.8$ and $\xi = 0.4$, respectively.

Section 4 then discusses for $\xi \in [\frac{1}{3}, 3]$ when successive (pre)images of the boxes $\mathcal{B}$ and $\mathcal{D}$ overlap in the relevant direction of projection, and how this relates to the existence of a blender. In Sec. 5, we discuss our results and point out avenues of ongoing and future research.

2 The box and its preimages for $\xi > 1$

We first consider H with $\xi > 1$, in which case the stable manifolds $W^s(p^{\pm})$ and $W^s(\Lambda)$ have dimension one. We consider the square $[-Q, Q] \times [-Q, Q]$ in the (x, y)-plane with the four points $(\pm Q, \pm Q)$, where

$$Q := \frac{1}{2}\left(1 + \beta + \sqrt{(1+\beta)^2 - 4\mu}\right). \tag{4}$$

Note that this square only depends on the parameters β and μ of the Hénon map, and that it always contains the two fixed points $p^{\pm}$; for our choice of $\mu = -9.5$ and $\beta = 0.3$, we have $Q = 3.8$.

We now define for $\xi > 1$ the box $\mathcal{B}$ in (x, y, z)-space as the parallelepiped given by the corner points

$$\bigcirc: \qquad \left(\pm Q,\ -Q,\ -\frac{Q}{\xi - 1} \cdot \frac{2 - \xi}{\xi}\right), \tag{5}$$

$$\diamond: \qquad \left(\pm Q,\ -Q,\quad \frac{Q}{\xi - 1}\right), \tag{6}$$

$$\square: \qquad \left(\pm Q,\quad Q,\ -\frac{Q}{\xi - 1}\right), \tag{7}$$

$$\triangle: \qquad \left(\pm Q,\quad Q,\quad \frac{Q}{\xi - 1} \cdot \frac{2 - \xi}{\xi}\right). \tag{8}$$

Hence, each of the symbols $\bigcirc$, $\diamond$, $\square$ and $\triangle$ indicates a pair of corner points with the same y- and z-coordinates, and we will use these symbols also to denote the respective edges of $\mathcal{B}$ between these points. The edges $\bigcirc$, $\diamond$, $\square$ and $\triangle$ are given by $x \in [-Q, Q]$ and, hence, are parallel to the x-axis.

By construction, $\mathcal{B}$ has the following properties.

- $\mathcal{B}$ projects in the z-direction onto the square $[-Q, Q] \times [-Q, Q]$.
- each intersection of $\mathcal{B}$ with a vertical plane of constant y is a rectangle with edges parallel to the x- and z-axes.
- each intersection of $\mathcal{B}$ with a vertical plane of constant x is a parallelogram with two vertical edges.

Moreover, the box $\mathcal{B}$ with Q as defined in (4) is tight with respect to the action of the inverse H^{-1}. By this we mean that its preimage satisfies the following statements, which can be checked directly from (4)–(8) and (1). Note here that, since $\xi > 1$, the x-direction of $\mathcal{B}$ is expanded, while its y- and z-directions are contracted under H^{-1}.

- The three-dimensional horseshoe-like set $H^{-1}(\mathcal{B})$ intersects $\mathcal{B}$ in two sub-boxes $\mathcal{B}_-$ with negative y and $\mathcal{B}_+$ with positive y. We will refer to $\mathcal{B}_-$ and $\mathcal{B}_+$ simply as the two (first) preimages of $\mathcal{B}$.
- The preimages $\mathcal{B}_-$ and $\mathcal{B}_+$ intersect the boundary of $\mathcal{B}$ only on its two faces with $x = -Q$ and $x = Q$, respectively.

- Vertical edges (parallel to the z-axis) of $\mathcal{B}$ map under H^{-1} to vertical edges of $H^{-1}(\mathcal{B})$; hence, the sub-boxes $\mathcal{B}_\pm$ have vertical edges that map to vertical edges of $\mathcal{B}$ under H.
- The outer vertical edges of $\mathcal{B}_-$ and $\mathcal{B}_+$ with $x = -Q$ are subsets of the respective vertical edge of $\mathcal{B}$; moreover, the two corner points $\left(\pm Q, Q, -\frac{Q}{\xi-1}\right)$ of $\mathcal{B}$ map as follows:

$$\begin{aligned} H^{-1}\left(Q, Q, -\frac{Q}{\xi-1}\right) &= \left(-Q, Q, -\frac{Q}{\xi-1}\right) \text{ and} \\ H^{-1}\left(-Q, Q, -\frac{Q}{\xi-1}\right) &= \left(-Q, -Q, -\frac{Q}{\xi-1}\cdot\frac{2-\xi}{\xi}\right). \end{aligned}$$

- The two (respective pieces of the) preimages of the edge $\diamond$ lie in the top face of $\mathcal{B}$, and those of the edge $\square$ lie in the bottom face of $\mathcal{B}$.
- The fixed points p^- and p^+ lie in $\mathcal{B}_-$ and $\mathcal{B}_+$, respectively.

Figure 1 shows the parallelepiped $\mathcal{B}$ for $\xi = 1.2$ together with its preimages $\mathcal{B}_-$ and $\mathcal{B}_+$; also shown is the diagonal plane $\Sigma := \{(x, y, z) \,|\, x = y\}$ containing the fixed points $p^\pm$, and the viewpoint is chosen such that the face of $\mathcal{B}$ with $x = Q$ is at the front of the image. Figure 1 illustrates the properties of the box $\mathcal{B}$ as well as of the preimages $\mathcal{B}_-$ and $\mathcal{B}_+$ inside $\mathcal{B}$. Each of these boxes is represented by its edges with the faces coloured and transparent. In particular, notice how $\mathcal{B}_-$ and $\mathcal{B}_+$ extend all the way across $\mathcal{B}$, meaning that they connect the faces of $\mathcal{B}$ with $x = \pm Q$; here, the edges of these sub-boxes form (approximate) parallelograms, whose sides are straight but whose top and bottom are slightly curved. Notice further that at $x = -Q$ the outer vertical edges of $\mathcal{B}_-$ and $\mathcal{B}_+$ are indeed subsets of the vertical edges of $\mathcal{B}$ and include the respective bottom corner point, while the inner vertical edges of $\mathcal{B}_-$ and $\mathcal{B}_+$ reach the upper edge of this face of $\mathcal{B}$. The three-dimensional nature of Figure 1 is enhanced by the inclusion of the intersection sets of $\mathcal{B}$ and $\mathcal{B}_\pm$ with the diagonal section Σ, which are the shown (approximate) parallelograms. Overall, this image shows that $\mathcal{B}$ is indeed the tightest parallelepiped with a square 'footprint' in the (x, y)-plane that yields a three-dimensional horseshoe, meaning that the sub-boxes $\mathcal{B}_\pm \subset \mathcal{B}$ intersect only the front and back faces with $x = \pm Q$. We remark that if the value of Q in (5)–(8) is increased from the one given in (4) then one still has a three-dimensional horseshoe but it is no longer tight. On the other hand, if Q is decreased, the set $H^{-1}(\mathcal{B})$ no longer intersects $\mathcal{B}$ as required to obtain a horseshoe.

Figure 1 also shows how the respective edges and corner points of $\mathcal{B}_-$ and $\mathcal{B}_+$ inherit the labels $\bigcirc$, $\diamond$, $\square$ and $\triangle$ from the respective x-aligned edges of $\mathcal{B}$ that they map to. We refer to these labeled edges as the *determining edges* of each box, because they are the ones that are expanded by H^{-1} in the three-dimensional horseshoe construction. Owing to the nonlinear nature of the map H, the determining edges of $\mathcal{B}_\pm$ are no longer straight lines that are parallel to the x-axis. Nevertheless, they are still aligned with the x-axis, by which we mean that the angle between the tangent at any point of the edges $\bigcirc$, $\diamond$, $\square$ and $\triangle$ with the vector $(1, 0, 0)$ is small. In particular, the sub-boxes $\mathcal{B}_\pm$ intersect the faces of $\mathcal{B}$ with $x = \pm Q$ in (approximate) parallelograms; the same is true for any transverse plane, such as the diagonal plane Σ in Fig. 1.

The overall geometry of the images of $\mathcal{B}$ under H^{-1} and H^{-2} is shown in Fig. 2. Panel (a) shows in (x, y, z)-space the box $\mathcal{B}$, its first preimages $\mathcal{B}_-$ and $\mathcal{B}_+$, and its second preimages $\mathcal{B}_{--}, \mathcal{B}_{-+} \subset \mathcal{B}_-$ and $\mathcal{B}_{+-}, \mathcal{B}_{++} \subset \mathcal{B}_+$. These boxes are again represented by their edges with their faces coloured and transparent; compare with Fig. 1. In particular, the four sub-boxes $\mathcal{B}_{\pm\mp}$ in Fig. 2(a) also connect the faces of $\mathcal{B}$ with $x = \pm Q$, where they intersect in (approximate) parallelograms that are 'steeper' and more sheared than those for $\mathcal{B}_\pm$; by this we mean that the angle of their non-vertical (slightly curved) edges with the y-direction is now larger. The top view in Fig. 2(b) shows that these sub-boxes correspond to increasingly thinner strips in

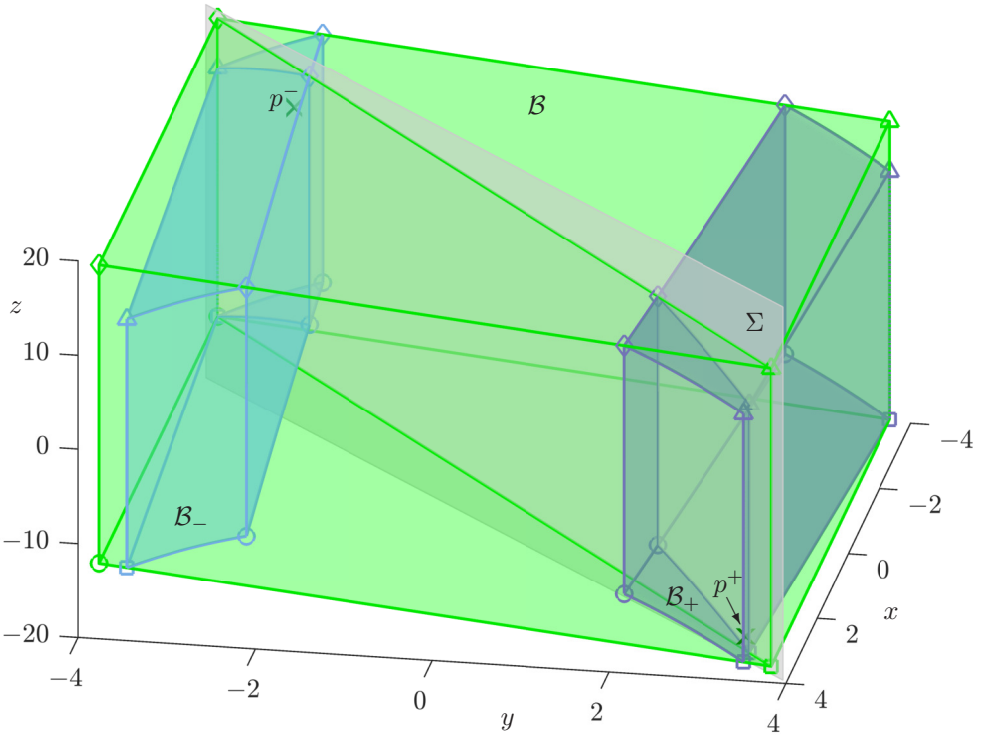

Figure 1: The box $\mathcal{B}$ (green) and its preimages $\mathcal{B}_-$ (light blue) and $\mathcal{B}_+$ (dark blue) under H with $\xi = 1.2$. The x-aligned edges of $\mathcal{B}_\pm$ are labelled $\bigcirc$, $\diamond$, $\square$ and $\triangle$ by their corner points according to how they map under H to the respective edges of $\mathcal{B}$ defined in (5)–(8). Also shown are the saddle fixed points $p^\pm$ (green crosses) contained in the diagonal plane Σ (gray); throughout $\mu = -9.5$ and $\beta = 0.3$.

the (x, y)-plane whose limit is the local stable manifold $W^s(\Lambda_h) \cap ([-Q, Q] \times [-Q, Q])$ of the hyperbolic set Λ_h of the Hénon map h; this set is a Cantor set of curve segments for our choice of the parameters. Figure 2(a) also shows the diagonal section Σ with the intersection sets of all boxes, and they are illustrated further in Fig. 2(c) in a 'front view' in projection onto the (y, z)-plane. Notice, in particular, how the parallelograms and, hence, the different boxes they represent, become more sheared under taking successive preimages.

The affine three-dimensional blender-horseshoe construction [1, 8] is very special in that all edges remain parallel to the three axes. For the map H, on the other hand, only the vertical edges remain parallel to the z-direction when taking preimages. Indeed, the determining edges $\bigcirc$, $\diamond$, $\square$ and $\triangle$ of successive preimages of the box $\mathcal{B}$ are no longer straight lines parallel to the x-axis; moreover, we observe a shearing of the sub-boxes.

The box $\mathcal{B}$ and its intersection set $\mathcal{B} \cap \Sigma$, which is an exact parallelogram, are given explicitely from (5)–(8) and their stated properties. The further sub-boxes and their intersection sets shown in Fig. 2 are determined as follows. We represent the determining edges of $\mathcal{B}$ by 30 evenly spaced points; the edges $\bigcirc$, $\diamond$, $\square$ and $\triangle$ of $\mathcal{B}_-$ and $\mathcal{B}_+$ are then determined from the interpolation of the preimages of the respective 30 points. Due to the skew-product nature of H, this determines the side faces of these two sub-boxes. Their top and bottom faces, on the other hand, are curved; they are determined in the same way by computing the respective pieces of the preimages of two sets of equidistant lines on the top and bottom surfaces of $\mathcal{B}$, respectively, parallell to the determining edges and each again represented by 30 points. Interpolation of this data is then used to compute the approximate parallelograms $\mathcal{B}_- \cap \Sigma$ and $\mathcal{B}_+ \cap \Sigma$ and, in particular, the intersection points $\bigcirc$, $\diamond$, $\square$ and $\triangle$ of their determining edges. The same procedure is then

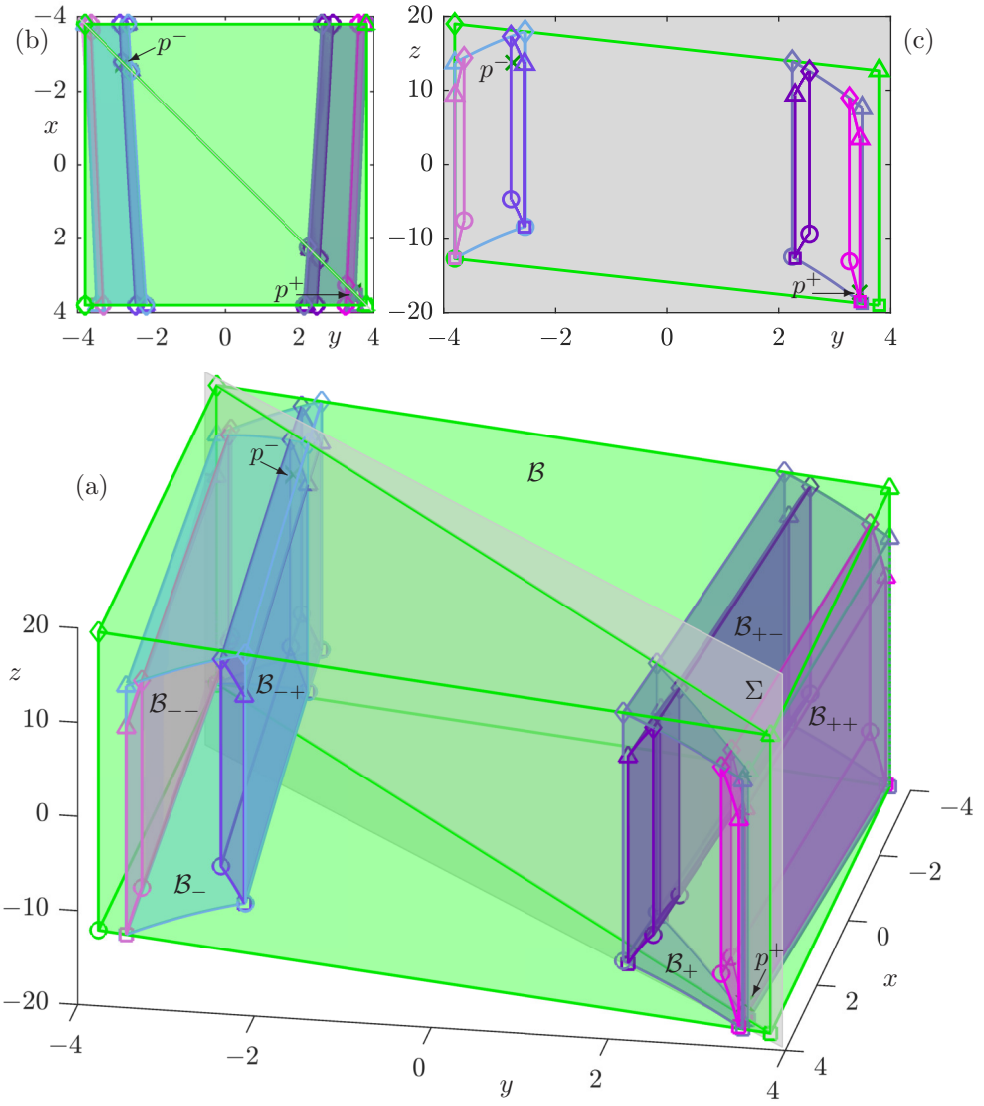

Figure 2: The box $\mathcal{B}$ (green) for $\xi = 1.2$ with its two preimages $\mathcal{B}_-$ (light blue) and $\mathcal{B}_+$ (dark blue) and their four preimages $\mathcal{B}_{--}$ (light magenta), $\mathcal{B}_{-+}$ (light purple), $\mathcal{B}_{+-}$ (purple) and $\mathcal{B}_{++}$ (magenta). Panel (a) shows these objects in (x, y, z)-space, together with $p^{\pm}$ (green crosses) and the diagonal plane Σ (gray). Panel (b) is the top view in the (x, y)-plane oriented as in panel (a), and panel (c) shows the intersecting (approximate) parallelograms in Σ; note that Σ is represented here by its projection onto the (y, z)-plane. Compare with Fig. 1.

applied to determine $\mathcal{B}_{--}$ and $\mathcal{B}_{-+}$ from $\mathcal{B}_-$, and $\mathcal{B}_{+-}$ and $\mathcal{B}_{++}$ from $\mathcal{B}_+$. In spite of the nonlinear nature of the sequence of sub-boxes in $\mathcal{B}$, the limiting set

$$\lim_{N\to\infty} \bigcap_{k=0}^{N} H^{-k}(\mathcal{B}) = W^s(\Lambda) \cap \mathcal{B} \tag{9}$$

exists, and the question is whether it has the carpet property and, hence, whether the hyperbolic set Λ of H is a blender. Theory suggests that Λ is a blender when $\xi > 1$ is sufficiently close to 1, while it is not a blender when ξ is sufficently large.

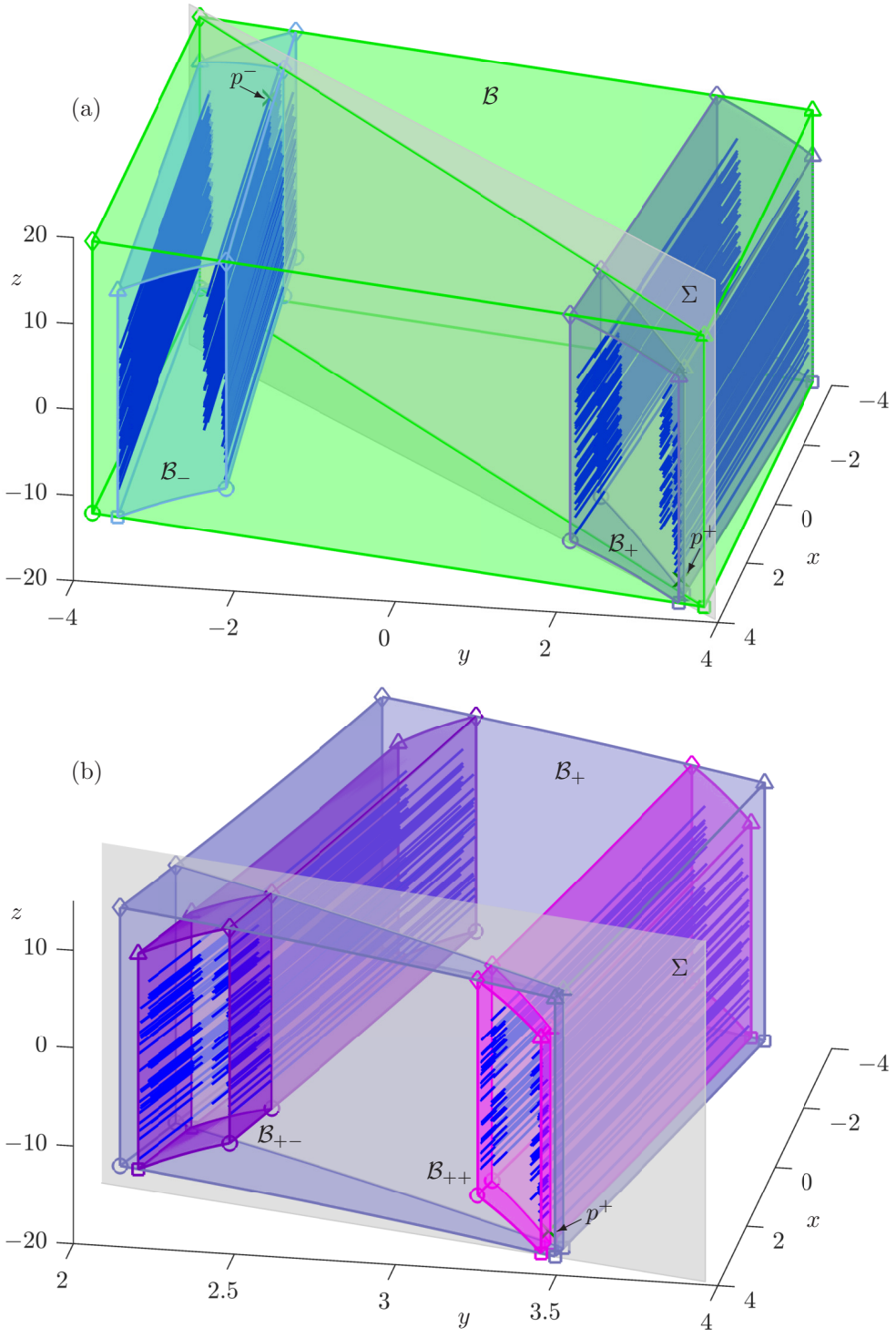

Figure 3: The first 450 segments of $W^s(p^\pm) \cap \mathcal{B}$ (blue curves) for $\xi = 1.2$, shown in panel (a) inside $\mathcal{B}$ (green), $\mathcal{B}_-$ (light blue) and $\mathcal{B}_+$ (dark blue), and in panel (b) inside $\mathcal{B}_+$ (dark blue), $\mathcal{B}_{+-}$ (purple) and $\mathcal{B}_{++}$ (magenta); also shown are $p^\pm$ (green crosses) and the diagonal plane Σ (gray).

2.1 The carpet property for $\xi = 1.2$

According to the results in [11, 12], for $\xi = 1.2$ the one-dimensional manifold $W^s(\Lambda) = \overline{W^s(p^\pm)}$ has the carpet property with respect to the y-direction and, hence, the hyperbolic set Λ of H is

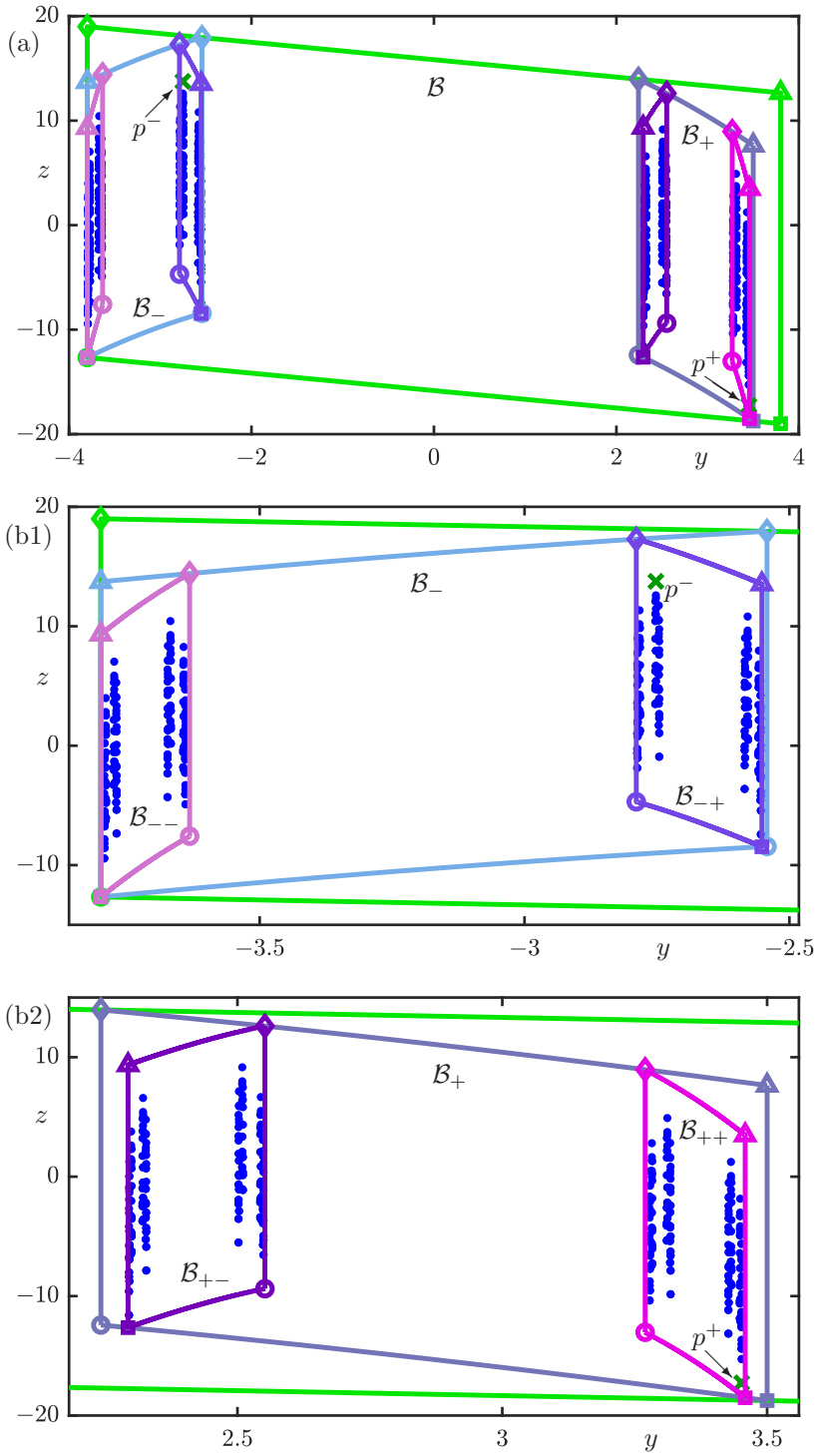

Figure 4: The first 900 intersection points in $W^s(p^{\pm}) \cap \Sigma$ for $\xi = 1.2$ shown together with $p^{\pm}$ and the intersection sets of $\mathcal{B}$ (green), $\mathcal{B}_-$ (light blue), $\mathcal{B}_+$ (dark blue), $\mathcal{B}_{--}$ (light magenta), $\mathcal{B}_{-+}$ (light purple), $\mathcal{B}_{+-}$ (purple) and $\mathcal{B}_{++}$ (magenta). Panel (a) shows all of $\Sigma \cap \mathcal{B}$, and panels (b1) and (b2) are enlargements of $\mathcal{B}_-$ and $\mathcal{B}_+$, respectively.

a blender. In the context of the three-dimensional horseshoe given by $\mathcal{B}$ and its preimages, this can be understood by the fact that there is sufficient overlap between the sub-boxes at every level $k \geq 1$ of (9) when they are seen along the y-direction. To illustrate the carpet property

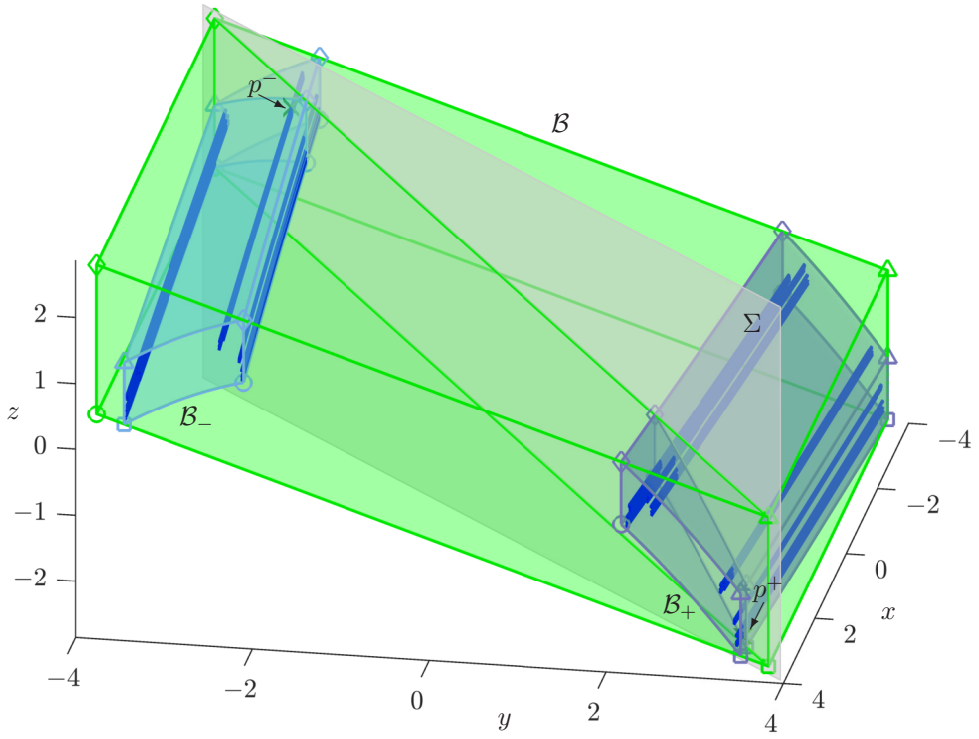

Figure 5: The stable manifolds $W^s(p^\pm)$ (blue curves) of $p^\pm$ (green crosses) for $\xi = 2.4$ inside the box $\mathcal{B}$ (green) and its two preimages $\mathcal{B}_-$ (light blue) and $\mathcal{B}_+$ (dark blue). Shown are the first 450 segments of $W^s(p^\pm) \cap \mathcal{B}$ in (x, y, z)-space together with $p^\pm$ (green crosses) and the diagonal plane Σ (gray). Compare with Fig. 3(a).

and how it is connected to properties of the preimages of the box $\mathcal{B}$, Fig. 3 illustrates how the stable manifolds $W^s(p^\pm)$ lies inside $\mathcal{B}$ and its preimages. To achieve this, we compute the stable manifolds $W^s(p^-)$ and $W^s(p^+)$ as parametrised curves up to considerable arclength, from which we determine and show in Fig. 3 the first 150 segments in $\mathcal{B}$ of the repeated intersections for each branch of $W^s(p^\pm)$. Specifically, these are both branches of $W^s(p^+)$ and one branch of $W^s(p^-)$ (its other branch goes straight to infinity and does not intersect $\mathcal{B}$ again); see [11, 12] for more details of the global structure of $W^s(p^\pm)$.

Figure 3(a) shows the computed 450 segments in $W^s(p^\pm) \cap \mathcal{B}$ with $\mathcal{B}$, $\mathcal{B}_-$ and $\mathcal{B}_+$, while panel (b) is an enlargement near $\mathcal{B}_+$ that also shows $\mathcal{B}_{+-}$ and $\mathcal{B}_{++}$. All segments in $W^s(p^\pm) \cap \mathcal{B}$ are aligned in the x-direction and connect the back and front faces of $\mathcal{B}$ where $x = \pm Q$; moreover, the segments can be seen to cluster successively in the sub-boxes $\mathcal{B}_-$ and $\mathcal{B}_+$, and $\mathcal{B}_{+-}$ and $\mathcal{B}_{++}$. By construction, when seen from the top along the z-direction, they form part of the Cantor set of curves $W^s(\Lambda_h) \cap ([-Q, Q] \times [-Q, Q])$. After taking k preimages of H, one can check in which sub-box a given segment lies to determine the symbolic sequence $s \in \{0, 1\}^{\mathbb{N}}$ that represents its location in this Cantor set of curve segments. In turn, each symbolic sequence $s \in \{0, 1\}^{\mathbb{N}}$ defines a unique one-dimensional segment of $W^s(\Lambda) \cap \mathcal{B}$.

When viewed side-on, on the other hand, the 450 computed segments in Fig. 3 seem to be very much distributed in their z-coordinate, and this suggests that $W^s(\Lambda) \cap \mathcal{B} = \overline{W^s(p^\pm) \cap \mathcal{B}}$ acts as a surface. This is illustrated further in Fig. 4 where we show the first 300 intersections points with Σ of each of the three repeatedly returning branches of $W^s(p^\pm)$; here, panel (a) shows the entirety of $\Sigma \cap \mathcal{B}$, while panels (b1) and (b2) are enlargements near $\mathcal{B}_-$ and $\mathcal{B}_+$, respectively. Indeed, the 900 points shown look dense in projection onto the z-axes. This observation was confirmed in [11, 12], where it is shown numerically that the (largest) gaps between the (finite

number of) projected points $W^s(p^\pm) \cap \Sigma$ goes to zero as the number of points in $W^s(p^\pm) \cap \Sigma$ increases.

Owing to the properties of the box $\mathcal{B}$, the symbolic sequence of a particular segment can be determined from that of its intersection point with a transverse section; see Fig. 4. Notice the self-similar nature of the construction (9) of taking the limit of successive preimages of $\mathcal{B}$. In particular, note that each segment of $W^s(\Lambda) \cap \Sigma$ has a unique z-value. In more colloquial terms, and as Fig. 3 illustrates, the set $W^s(\Lambda) \cap \mathcal{B} = \overline{W^s(p^\pm) \cap \mathcal{B}}$ is a set of (infinitely many) spaghetti that look like a Cantor set from the top and like a surface when seen side-on. This is the geometric essence of the carpet property. Specifically, the orthogonal projection of $W^s(p^\pm) \cap \Sigma$ onto the y-axis is always one and the same Cantor set associated with the Hénon map — while the orthogonal projection of $W^s(p^\pm) \cap \Sigma$ onto the z-axis fills up an interval [11, 12].

2.2 Lack of the carpet property for $\xi = 2.4$

In contrast, when $\xi = 2.4$ the manifold $W^s(\Lambda)$ does not have the carpet property according to the numerical convergence test for gaps in projection [11, 12]. Figure 5 shows the set $W^s(p^+) \cap \mathcal{B}$ and the boxes $\mathcal{B}$, $\mathcal{B}_-$ and $\mathcal{B}_+$ for this case, in the same way as Fig. 3(a). While the top views of these two figures is identical, Fig. 5 now shows a much 'thinner' set of spaghetti in $\mathcal{B}$ that does not look like a surface. This is confirmed by the respective intersection sets with the diagonal plane Σ, which is illustrated further in Fig. 6: the points $W^s(p^+) \cap \Sigma$ now appear to have gaps in the z-coordinate. Notice how the segments in $W^s(p^\pm) \cap \mathcal{B}$ and points in $W^s(p^\pm) \cap \Sigma$ cluster strongly in $\mathcal{B}_-$ and $\mathcal{B}_+$, and successively in $\mathcal{B}_{--}$ and $\mathcal{B}_{-+}$, $\mathcal{B}_{+-}$ and $\mathcal{B}_{++}$. As a result, in Fig. 6(a) the points in $W^s(p^\pm) \cap \Sigma$ are practically all obscured by the (approximate) parallelograms that are the intersetions sets of $\mathcal{B}_{--}$ and $\mathcal{B}_{-+}$, $\mathcal{B}_{+-}$ and $\mathcal{B}_{++}$ with Σ. The set $W^s(p^\pm) \cap \Sigma$ is, however, visible in the enlargement panels (b1) and (b2). The difference with the case $\xi = 1.2$ is that, for $\xi = 2.4$, the respective boxes no longer overlap fully: there is now a gap in the z-coordinate between the projections of $\mathcal{B}_-$ and $\mathcal{B}_+$, as well as of $\mathcal{B}_{+-}$ and $\mathcal{B}_{++}$; see Fig. 6(a) and (b2). This explains the visible gaps between points in $W^s(p^\pm) \cap \Sigma$ when seen in projection onto the z-coordinate. The boxes $\mathcal{B}_{--}$ and $\mathcal{B}_{-+}$ in panel (b1), on the other hand, still overlap.

3 The box and its preimages for $0 < \xi < 1$

When $0 < \xi < 1$ the unstable manifolds $W^u(p^\pm)$ and $W^u(\Lambda)$ are of dimension one, and we now consider images of a suitable box $\mathcal{D}$ under H. This box is also defined over the square $[-Q, Q] \times [-Q, Q]$ in the (x, y)-plane with Q as in (4), namely as the parallelepiped given by the corner points

$$\square: \qquad \left(-Q,\ \pm Q,\ -\frac{Q}{1-\xi}\right), \tag{10}$$

$$\triangle: \qquad \left(-Q,\ \pm Q,\quad \frac{Q}{1-\xi}\cdot(2\xi-1)\right), \tag{11}$$

$$\bigcirc: \qquad \left(\ \ Q,\ \pm Q,\ -\frac{Q}{1-\xi}\cdot(2\xi-1)\right), \tag{12}$$

$$\diamond: \qquad \left(\ \ Q,\ \pm Q,\quad \frac{Q}{1-\xi}\right). \tag{13}$$

Here, the symbols $\bigcirc$, $\diamond$, $\square$ and $\triangle$ again indicate the pairs of corner points and corresponding determining edges; these are now parallel to the y-axis, which is the expanding direction, while the x- and z-directions are contracted under H.

Figure 7 shows the parallelopid $\mathcal{D}$ (green) over the square $[-Q, Q] \times [-Q, Q]$ and its (forward) images $\mathcal{D}_-$ and $\mathcal{D}_+$; this illustrates that these boxes have the equivalent properties listed in Sec. 2

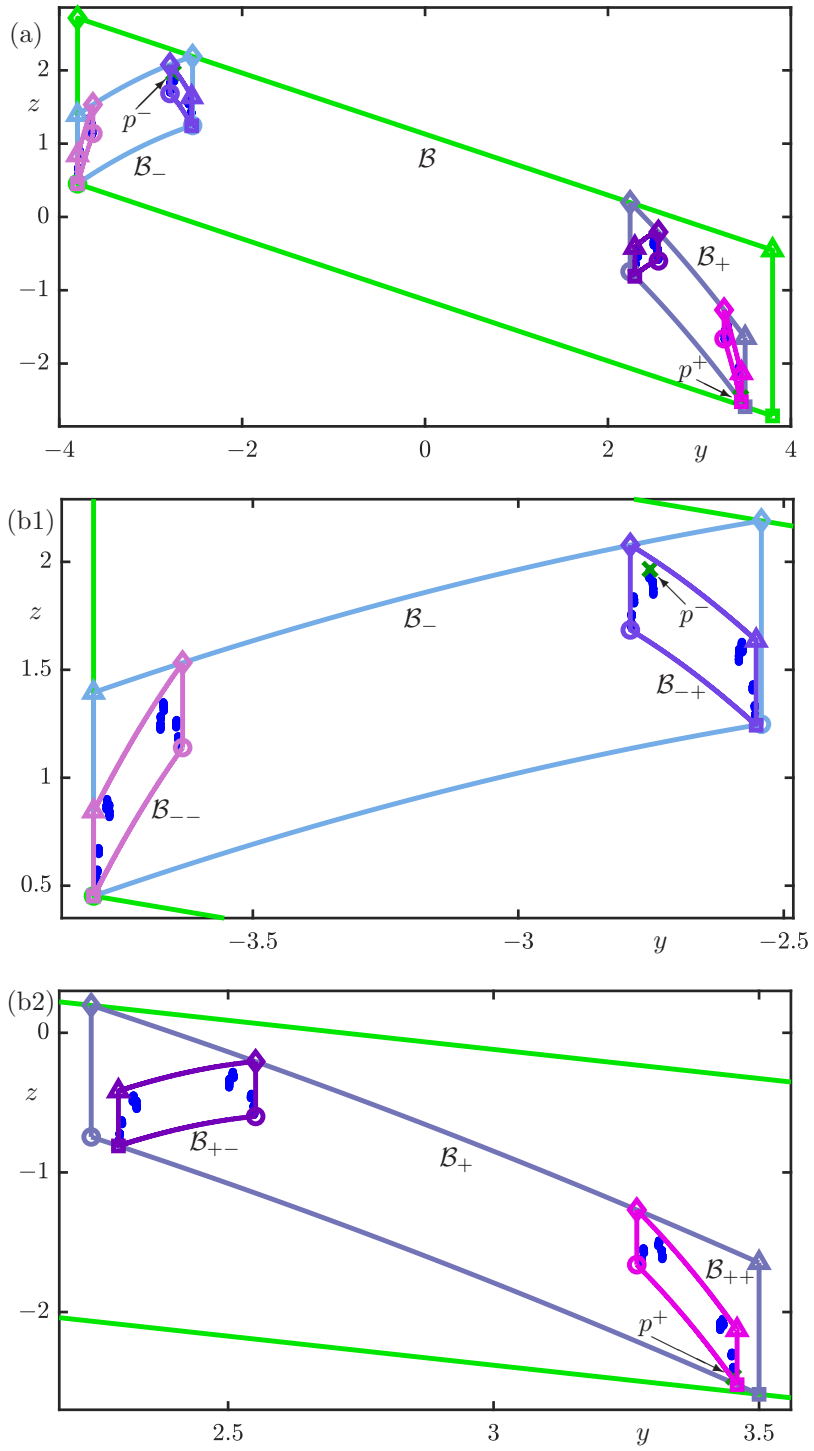

Figure 6: The first 900 intersection points $W^s(p^\pm) \cap \Sigma$ for $\xi = 2.4$ from Fig. 5 shown together with $p^\pm$ and the intersection sets of $\mathcal{B}$ (green), $\mathcal{B}_-$ (light blue), $\mathcal{B}_+$ (dark blue), $\mathcal{B}_{--}$ (light magenta), $\mathcal{B}_{-+}$ (light purple), $\mathcal{B}_{+-}$ (purple) and $\mathcal{B}_{++}$ (magenta). Panel (a) shows all of $\Sigma \cap \mathcal{B}$, and panels (b1) and (b2) are enlargements of $\mathcal{B}_-$ and $\mathcal{B}_+$, respectively.

for $\mathcal{B}$ and $\mathcal{B}_\pm$, subject to the reversal of the roles of the x- and y-directions. Namely, the sub-boxes $\mathcal{D}_-$ and $\mathcal{D}_+$ intersect the boundary of $\mathcal{D}$ only on the two faces given by $y = -Q$ and $y = Q$, respectively. With Q as given in (4), the box $\mathcal{D}$ is tight with respect to the action of H, meaning that now the outer edges of $\mathcal{D}_\pm$ are subsets of the outer edges of $\mathcal{D}$ with $y = Q$; moreover, the

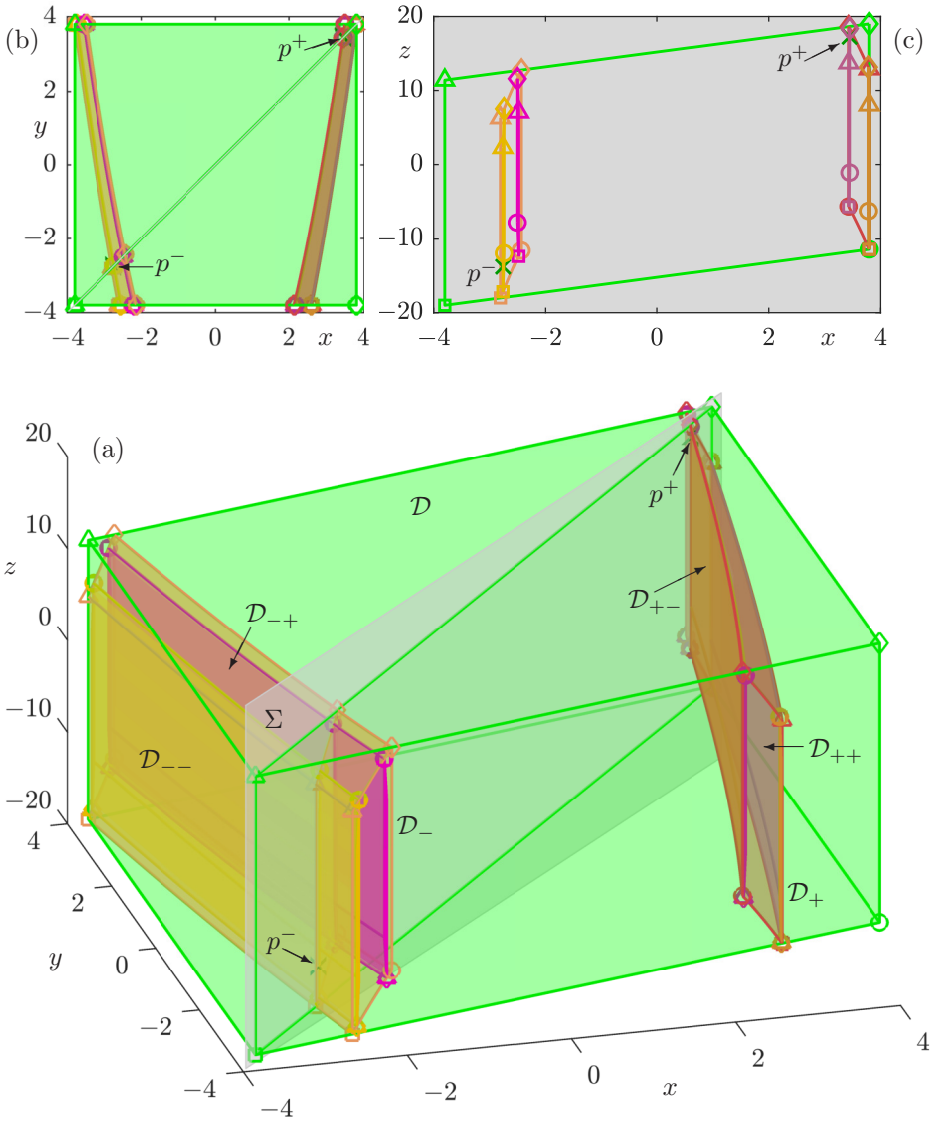

Figure 7: The box $\mathcal{D}$ (green), its images $\mathcal{D}_-$ (orange) and $\mathcal{D}_+$ (red), and their images $\mathcal{D}_{--}$ (yellow), $\mathcal{D}_{-+}$ (magenta), $\mathcal{D}_{+-}$ (dark magenta) and $\mathcal{D}_{++}$ (light brown) under H with $\xi = 0.8$. Panel (a) shows these objects in (x, y, z)-space together with $p^\pm$ (green crosses) and diagonal Σ (gray). Panel (b) is the top view in the (x, y)-plane, and panel (c) shows the intersecting parallelograms in Σ, which is represented by its projection onto the (x, z)-plane. The y-aligned determining edges are labeled $\square$, $\triangle$, $\bigcirc$ and $\diamond$ by their respective corner points, as defined for $\mathcal{D}$ in (10)–(13). Compare with Fig. 2.

two (respective pieces of the) images of the edges $\diamond$ and $\square$ lie in the top and bottom face of $\mathcal{D}$, respectively. These properties follow from the expressions (10)–(13) and formula (1) for H. Figure 7 also shows the four images $\mathcal{D}_{--}$, $\mathcal{D}_{-+}$, $\mathcal{D}_{+-}$ and $\mathcal{D}_{++}$ of $\mathcal{D}$ under H^2. Notice that these sub-boxes are very narrow in the x-direction and close to the respective boundaries of $\mathcal{D}_-$ and $\mathcal{D}_+$. This is due to the strong contraction of $\mathcal{D}$ in the x-direction under H, which is considerably stronger than that of $\mathcal{B}$ in the y-direction under H^{-1}; compare with Fig. 2.

As Fig. 7 illustrates, the nested sub-boxes also constitute a three-dimensional horseshoe, now

under the (forward) action of H, meaning that the limiting set

$$\lim_{N\to\infty} \bigcap_{k=0}^{N} H^k(\mathcal{D}) = W^u(\Lambda) \cap \mathcal{D} \tag{14}$$

exists and Λ is a blender when $W^u(\Lambda) \cap \mathcal{B}$ has the carpet property. Again, Λ is expected to be a blender when when $0 < \xi < 1$ is sufficiently close to 1, while it is not a blender when ξ is sufficently close to 0; see [11, 12].

3.1 The carpet property for $\xi = 0.8$

Figure 8 shows the unstable manifolds $W^u(p^\pm) \cap \mathcal{D}$ for $\xi = 0.8$ inside the box $\mathcal{D}$ and its images $\mathcal{D}_-$ and $\mathcal{D}_+$ in panel (a), while panel (b) illustrates the situation locally near $\mathcal{D}_-$ with the second images $\mathcal{D}_{--}$ and $\mathcal{D}_{-+}$. We again compute the manifolds $W^u(p^\pm)$ as curves and show the first 150 segments of the branches that intersect $\mathcal{D}$ repeatedly, which are both branches of $W^u(p^-)$ and one branch of $W^u(p^+)$ (its other branch goes straight to infinity). As a result of the strong contraction of the x-direction under H, the segments $W^u(p^\pm) \cap \mathcal{D}$ are seen to cluster strongly near the boundaries of $\mathcal{D}_-$ and $\mathcal{D}_+$, and near $\mathcal{D}_{--}$ and $\mathcal{D}_{-+}$, respectively. As a result, the Cantor structure of $W^u(\Lambda)$ is much harder to recognise in Fig. 8 compared to Fig. 3.

According to [11, 12], an orthogonal projection onto the z-coordinate for $\xi = 0.8$ shows gaps between the segments $W^u(p^\pm) \cap \mathcal{D}$ that converge to zero as more segments are added. Hence, $W^u(\Lambda)$ has the carpet property and Λ is a blender. Indeed, the 450 segments computed in Fig. 8 already give the impression that $W^u(p^\pm) \cap \mathcal{D}$ is dense in projection onto the (y, z)-plane. To illustrate this further, Fig. 9 shows the first 300 intersection points with the diagonal plane Σ of each of the three repeatedly returning branches of $W^u(p^\pm)$ together with the intersection sets of the sub-boxes from Fig. 8; here Fig. 9(a) shows all of $\mathcal{D}$, while panels (b1) and (b2) are enlargements near $\mathcal{D}_-$ and $\mathcal{D}_+$, respectively. The 900 points of $W^u(p^\pm) \cap \Sigma$ do not appear to have any gaps between them (at this resolution) when projected onto the z-axis. This is owing to the fact that the sub-boxes $\mathcal{D}_-$ and $\mathcal{D}_+$, and $\mathcal{D}_{--}$, $\mathcal{D}_{-+}$, $\mathcal{D}_{+-}$ and $\mathcal{D}_{++}$ overlap sufficiently, meaning that they do not leave gaps when seen in projection onto the z-coordinate. Notice that $\mathcal{D}_{--}$, $\mathcal{D}_{-+}$, $\mathcal{D}_{+-}$ and $\mathcal{D}_{++}$ are so narrow that they would obscure $W^u(p^\pm) \cap \Sigma$ in Fig. 9; this is why we now plot these points 'on top' of the shown boundaries of these sub-boxes.

3.2 Lack of the carpet property for $\xi = 0.4$

Figures 10 and 11 illustrate that Λ is not a blender when $\xi = 0.4$ according to the convergence test in [11, 12]. When seen along the x-axis, the shown segments of $W^u(p^\pm) \cap \mathcal{D}$ in Fig. 10 now appear to be a Cantor set of curves, which suggests that $W^u(\Lambda)$ no longer has the carpet property. Figure 11 illustrates this further by showing how the points in $W^u(p^\pm) \cap \Sigma$ sit with the different sub-boxes. Notice in panel (a) how narrowly spaced these points are in the very narrow $\mathcal{D}_{--}$, $\mathcal{D}_{-+}$, $\mathcal{D}_{+-}$ and $\mathcal{D}_{++}$, which lie near the boundaries of the sub-boxes $\mathcal{D}_-$ and $\mathcal{D}_+$. The enlargements in panels (b1) and (b2) show that, in turn, the points in $W^u(p^\pm) \cap \Sigma$ lie close to the boundaries of $\mathcal{D}_{--}$, $\mathcal{D}_{-+}$, $\mathcal{D}_{+-}$ and $\mathcal{D}_{++}$; specifically, in such a way that there are gaps in between these groups of points in terms of their z-coordinates. Notice from Fig. 11 that the respective pairs of sub-boxes shown in each panel do not overlap in projection onto the z-axis, meaning that this projection of $W^u(\Lambda) \cap \Sigma$ is now also a Cantor set that is topologically a full shift on two symbols. This shows in a different way that Λ is indeed not a blender for $\xi = 0.4$.

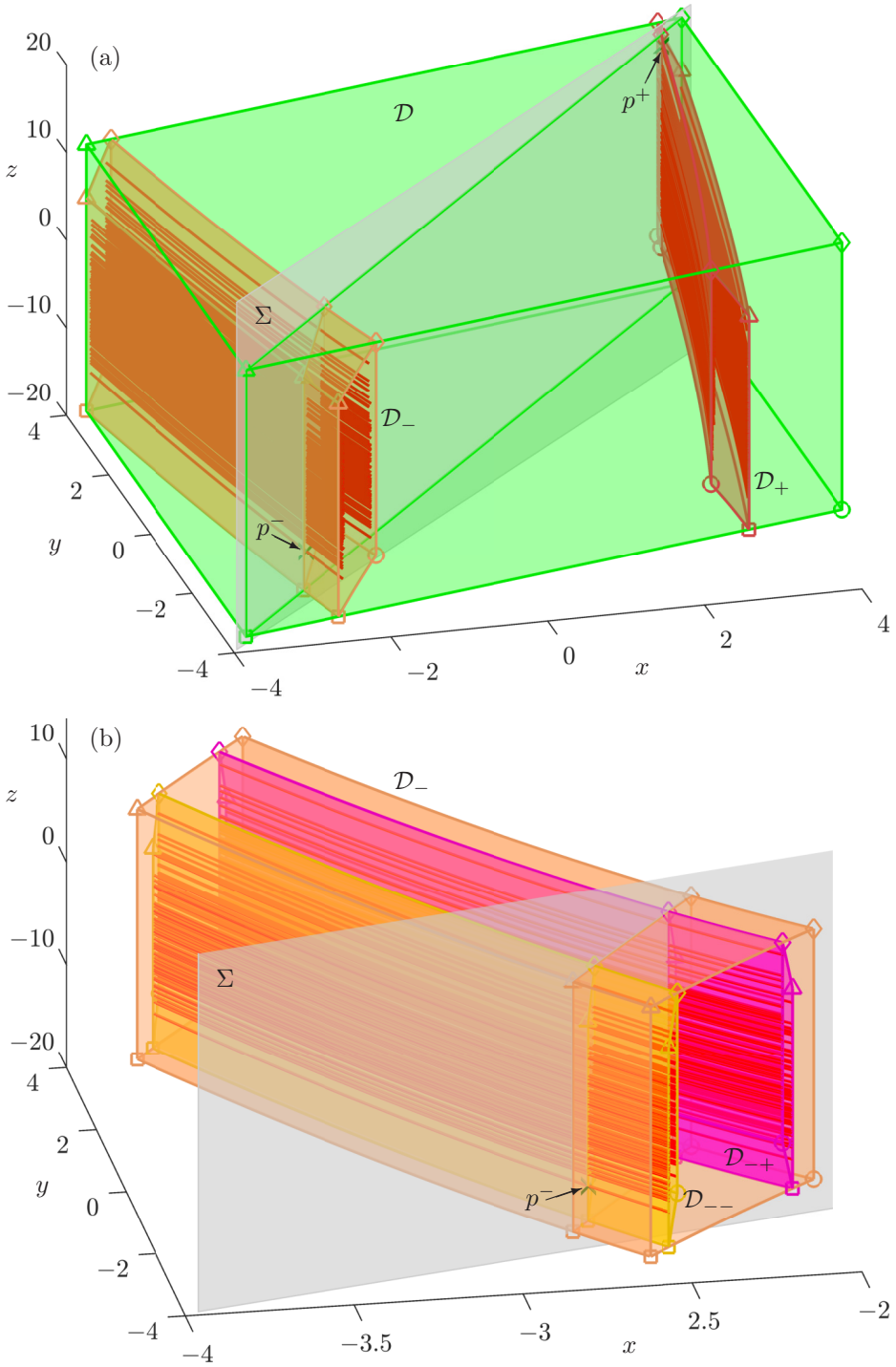

Figure 8: The first 450 segments of $W^u(p^{\pm}) \cap \mathcal{D}$ (blue curves) for $\xi = 0.8$, shown in panel (a) inside $\mathcal{D}$ (green), $\mathcal{D}_-$ (orange) and $\mathcal{D}_+$ (red), and in panel (b) inside $\mathcal{D}_-$ (orange), $\mathcal{D}_{--}$ (yellow) and $\mathcal{D}_{-+}$ (magenta); also shown are $p^{\pm}$ (green crosses) and the diagonal plane Σ (gray).

4 Relative positions of determining edges

Figures 4 and 6 of the intersection sets in the diagonal plane Σ illustrate that the carpet property of $W^s(\Lambda)$ for $\xi > 1$ is associated with the overlap in the z-coordinate between sub-boxes in the sequence defining the limiting set in (9). Similarly and according to Figs. 9 and 11, the carpet

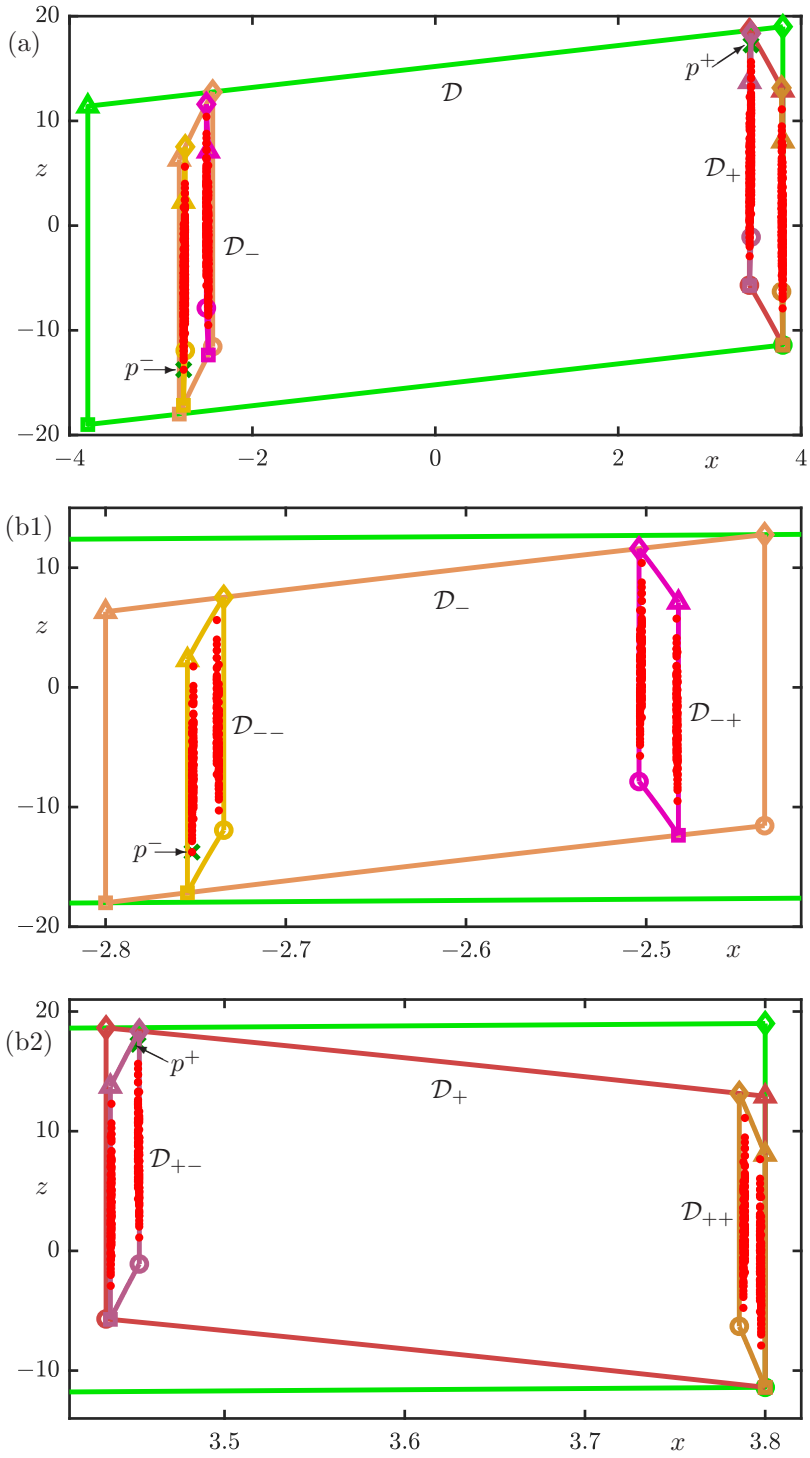

Figure 9: The first 900 intersection points $W^u(p^{\pm}) \cap \Sigma$ for $\xi = 1.2$ from Fig. 8 shown together with $p^{\pm}$ and the intersection sets of $\mathcal{D}$ (green), $\mathcal{D}_-$ (orange), $\mathcal{D}_+$ (red), $\mathcal{D}_{--}$ (yellow), $\mathcal{D}_{-+}$ (magenta), $\mathcal{D}_{+-}$ (dark magenta) and $\mathcal{D}_{++}$ (light brown). Panel (a) shows all of $\Sigma \cap \mathcal{D}$ and panels (b1) and (b2) are enlargements of $\mathcal{D}_-$ and $\mathcal{D}_+$, respectively.

propety of $W^u(\Lambda)$ for $0 < \xi < 1$ is associated with the overlap in the z-coordinate between sub-boxes that generate the limiting set in (14). We now investigate further how the respective z-overlap between $H^{-k}(\mathcal{B}) \cap \Sigma$ and $H^k(\mathcal{D}) \cap \Sigma$ in the particular plane Σ of intersection relates

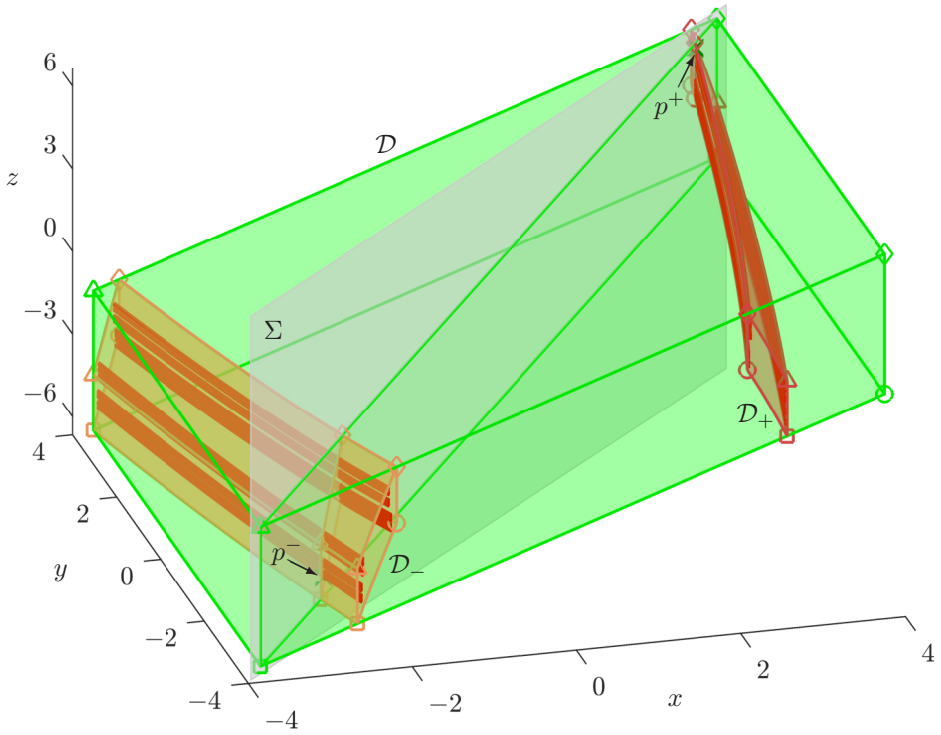

Figure 10: The unstable manifolds $W^u(p^\pm)$ (red curves) of $p^\pm$ (green crosses) for $\xi = 0.4$ inside the box $\mathcal{D}$ (green) and its two preimages $\mathcal{D}_-$ (orange) and $\mathcal{D}_+$ (red). Shown are the first 450 segments of $W^u(p^\pm) \cap \mathcal{B}$ in (x, y, z)-space together with the diagonal plane Σ (gray). Compare with Fig. 8.

to the properties of $W^s(\Lambda) \cap \Sigma$ and $W^u(\Lambda) \cap \Sigma$, respectively. To this end, we consider how these objects change with the contraction rate ξ over the range $[\frac{1}{3}, 3]$. Since the corresponding z-ranges vary a lot with ξ, it is convenient to show the relevant information in the compactfied coordinate $\bar{z}$, which is obtained by the transformation

$$\bar{z} := \frac{z}{1 + |z|} \in [-1, 1]. \tag{15}$$

Moreover, for ease of comparison of the two cases $0 < \xi < 1$ and $\xi > 1$, we transform the smaller interval $[\frac{1}{3}, 1]$ to the interval $[-1, 1]$ so that it has length 2 as well; this is achieved by the transformation

$$\xi \to -\frac{1}{\xi} + 2. \tag{16}$$

Figure 12 shows the $\bar{z}$-values $\bigcirc_{\bar{z}}(\xi)$, $\diamond_{\bar{z}}(\xi)$, $\square_{\bar{z}}(\xi)$ and $\triangle_{\bar{z}}(\xi)$ of the intersection points with Σ of the determining edges of the pairs of sub-boxes $\mathcal{B}_\pm$ and $\mathcal{D}_\pm$ in panel (a), and of the four respective sub-boxes $\mathcal{D}_{\pm\mp}$ and $\mathcal{B}_{\pm\mp}$ in panel (b). These points form ξ-parametrised curves in the $(\xi, \bar{z})$-plane, which are labelled by the respective symbol and have the colour of the corresponding box as in previous figures. To obtain these curves, we consider 500 evenly spaced ξ-values in $[0.001, 0.999]$ and 450 evenly spaced ξ-values in $[1.01, 8.0]$, for which the intersection points of the respective determining edges with Σ are computed by interpolation from (pre)images of H as was explained in Sec. 2.

Figure 12 also shows the $\bar{z}$-values of the intersection sets $W^u(p^\pm) \cap \Sigma$ for $0 < \xi < 1$ and $W^s(p^\pm) \cap \Sigma$ for $\xi > 1$. They form the gray background and consist of curves generated from computed intersection points. Specifically, the respective one-dimensional manifolds were computed for $\xi \in \{0.01, 0.1, 0.2, 0.3, 0.35, 0.5, 0.6, 1.7, 1.8, 1.9, 2, 2.1, 2.4, 4.0, 10.0, 50.0, 100.0\}$; the

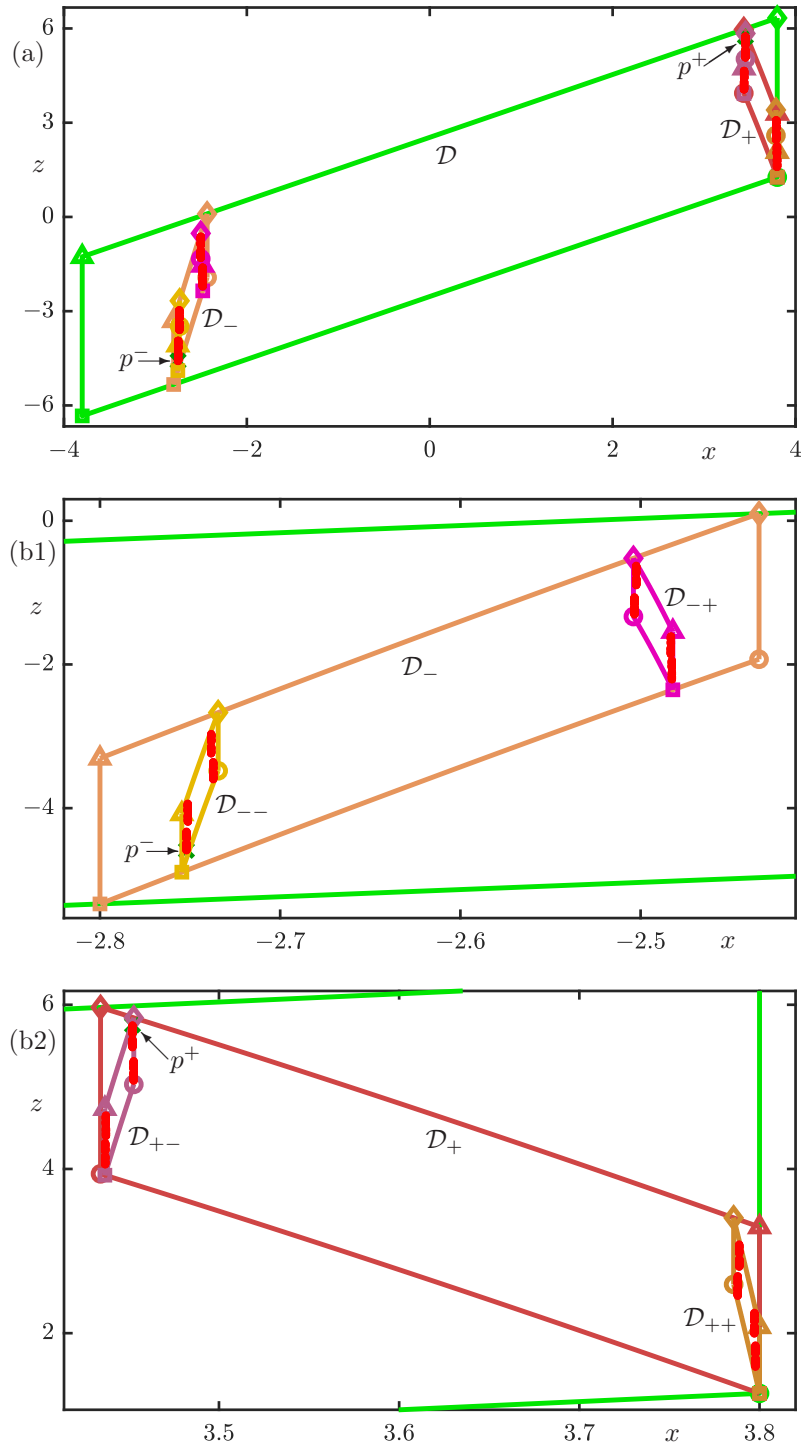

Figure 11: The first 900 intersection points $W^u(p^\pm) \cap \Sigma$ for $\xi = 0.4$ from Fig. 10 shown together with $p^\pm$ and the intersection sets of $\mathcal{D}$ (green), $\mathcal{D}_-$ (orange), $\mathcal{D}_+$ (red), $\mathcal{D}_{--}$ (yellow), $\mathcal{D}_{-+}$ (magenta), $\mathcal{D}_{+-}$ (dark magenta) and $\mathcal{D}_{++}$ (light brown). Panel (a) shows all of $\Sigma \cap \mathcal{D}$, and panels (b1) and (b2) are enlargements of $\mathcal{D}_-$ and $\mathcal{D}_+$, respectively.

first 1,000 intersection points for $\xi \leq 4$ and the first 500 intersection points for $\xi \geq 4$ were determined for each returning branch of manifold. These points were then connected by using modified Akima interpolation in Matlab to obtain a set of gray ξ-parametrised curves over the ξ-range $[\frac{1}{3}, 3]$. Moreover, in the range $\xi \in [0.6, 1.7]$, the area between the $\bar{z}$-values of $p^\pm$

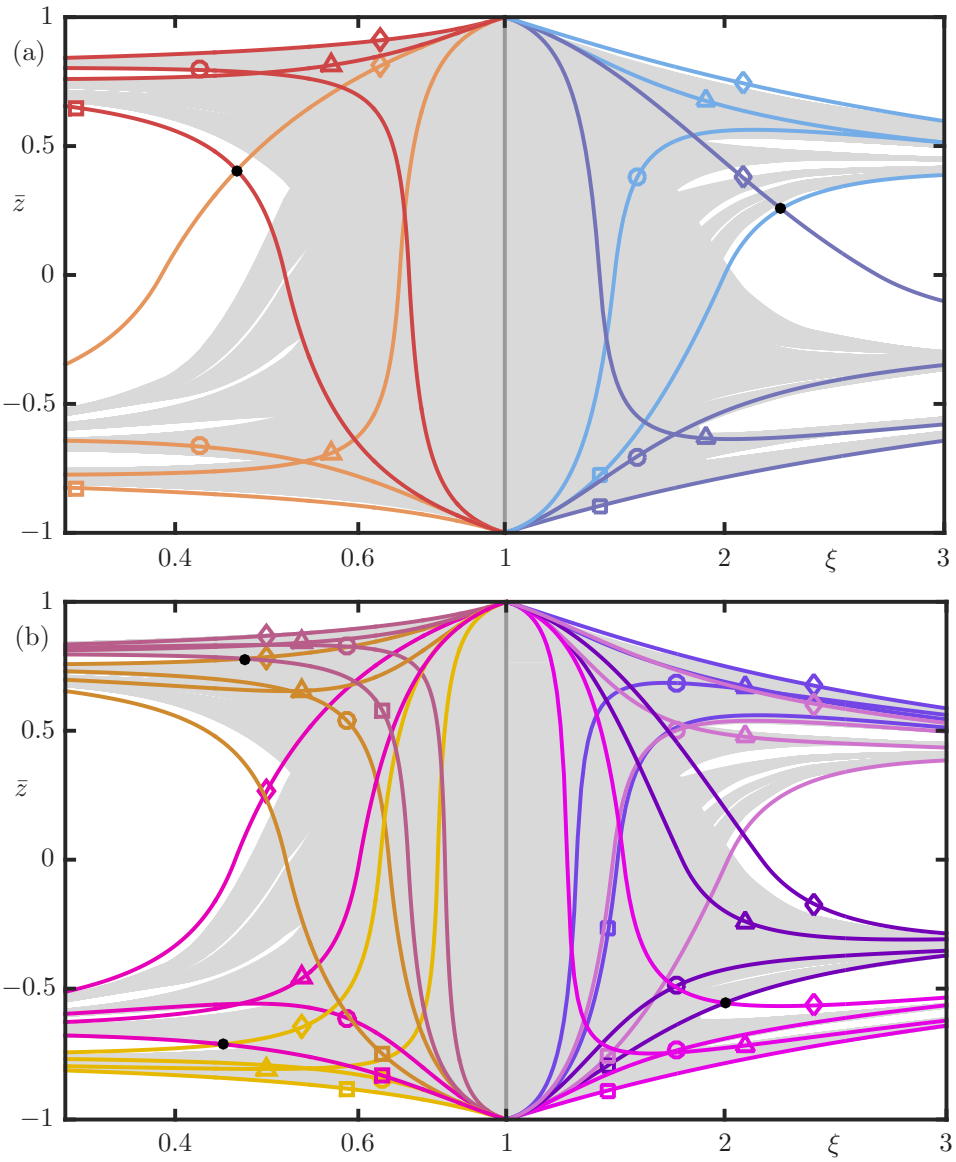

Figure 12: The curves $\bigcirc_{\bar{z}}(\xi)$, $\diamond_{\bar{z}}(\xi)$, $\square_{\bar{z}}(\xi)$ and $\triangle_{\bar{z}}(\xi)$ for the sub-boxes $\mathcal{B}_{\pm}$ and $\mathcal{D}_{\pm}$ in panel (a), and for the sub-boxes $\mathcal{D}_{\pm\mp}$ and $\mathcal{B}_{\pm\mp}$ in panel (b), shown in the $(\xi, \bar{z})$-plane with $[\frac{1}{3}, 1]$ rescaled by (16) to have width 2. Colours match those of the boxes in Figs. 4, 6, 9 and 11, and the gray background is formed by $W^u(p^{\pm}) \cap \Sigma$ for $\xi \in [\frac{1}{3}, 1)$ and $W^s(p^{\pm}) \cap \Sigma$ for $\xi \in (1, 3]$. Black dots mark the intersection points of $\diamond_{\bar{z}}(\xi)$ and $\square_{\bar{z}}(\xi)$ of opposing sub-boxes, which indicate a gain/loss of overlap.

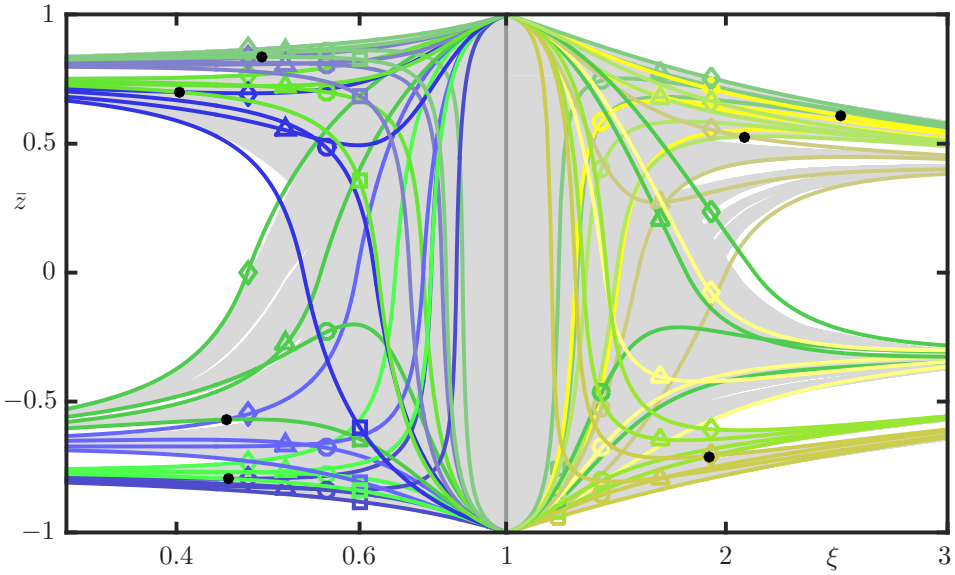

Figure 13: The curves $\bigcirc_{\bar{z}}(\xi)$, $\diamond_{\bar{z}}(\xi)$, $\square_{\bar{z}}(\xi)$ and $\triangle_{\bar{z}}(\xi)$ for the sub-boxes $\mathcal{D}_{\pm\mp\pm}$ and $\mathcal{B}_{\pm\mp\pm}$; shown with $W^u(p^\pm) \cap \Sigma$ and $W^s(p^\pm) \cap \Sigma$ as in Fig. 12.

was gray-filled, since there are no visible gaps (in this projection) at the scale of these figures; compare with [12, Fig. 8].

Notice in Fig. 12 that the different curves $\bigcirc_{\bar{z}}(\xi)$, $\diamond_{\bar{z}}(\xi)$, $\square_{\bar{z}}(\xi)$ and $\triangle_{\bar{z}}(\xi)$ align quite well with the 'boundaries' of $W^u(p^\pm) \cap \Sigma$ and $W^s(p^\pm) \cap \Sigma$. It is noticeable that the curves for $\mathcal{D}_{\pm\mp}$ and $\mathcal{B}_{\pm\mp}$ in panel (b) lie closer to $W^u(p^\pm) \cap \Sigma$ and $W^s(p^\pm) \cap \Sigma$, respectively, than those for $\mathcal{B}_\pm$ and $\mathcal{D}_\pm$ in panel (a). Importantly, intersection points between curves $\diamond_{\bar{z}}(\xi)$ and $\square_{\bar{z}}(\xi)$ of pairs of sub-boxes correspond to changes in their overlap properties as identified in Figs. 4 and 6 for $\xi > 1$, and Figs. 9 and 11 for $0 < \xi < 1$. As expected from these figures, there are two intersection points in Fig. 12(a) between the respective curves $\diamond_{\bar{z}}(\xi)$ and $\square_{\bar{z}}(\xi)$. Namely $(\xi, \bar{z}) \approx (0.4506, 0.4061)$ marks the gain or loss of overlap between the sub-boxes $\mathcal{D}_-$ and $\mathcal{D}_+$, and $(\xi, \bar{z}) \approx (2.258, 0.2566)$ marks that between $\mathcal{B}_-$ and $\mathcal{B}_+$.

Figure 12(b) shows the curves $\bigcirc_{\bar{z}}(\xi)$, $\diamond_{\bar{z}}(\xi)$, $\square_{\bar{z}}(\xi)$ and $\triangle_{\bar{z}}(\xi)$ for the sub-boxes $\mathcal{B}_{\pm\mp}$ and $\mathcal{D}_{\pm\mp}$. For $0 < \xi < 1$ there are two intersection points between curves $\diamond_{\bar{z}}(\xi)$ and $\square_{\bar{z}}(\xi)$, namely the point $(\xi, \bar{z}) \approx (0.4377, -0.7094)$ concerning overlap between $\mathcal{D}_{--}$ and $\mathcal{D}_{-+}$, and the point $(\xi, \bar{z}) \approx (0.4566, 0.7803$ concerning overlap between $\mathcal{D}_{+-}$ and $\mathcal{D}_{++}$. The fact that both these points occur between $\xi = 0.8$ and $\xi = 0.4$ reflects the change in overlap observed between Figs. 9 and 11. For $\xi > 1$, on the other hand, Fig. 12(b) shows only the intersection point $(\xi, \bar{z}) \approx (1.9883, -0.5498)$ between the respective curves $\diamond_{\bar{z}}(\xi)$ and $\square_{\bar{z}}(\xi)$ that marks the change in overlap between $\mathcal{B}_{+-}$ and $\mathcal{B}_{++}$. There is no intersection point between the the curves $\diamond_{\bar{z}}(\xi)$ for $\mathcal{B}_{--}$ and $\square_{\bar{z}}(\xi)$ for $\mathcal{B}_{-+}$ in the shown ξ-range. Moreover, we did not find such an intersection point based on the data we computed in $[1.01, 8.0]$; so if it exists, this point will lie well beyond $\xi = 8.0$. In other words, $\mathcal{B}_{--}$ and $\mathcal{B}_{-+}$ remain in overlap, which agrees with the observed change between Figs. 4 and 6.

The curves $\bigcirc_{\bar{z}}(\xi)$, $\diamond_{\bar{z}}(\xi)$, $\square_{\bar{z}}(\xi)$ and $\triangle_{\bar{z}}(\xi)$ can be computed for further (pre)images, and Fig. 13 shows them for the respective eight sub-boxes $\mathcal{D}_{\pm\mp\pm}$ and $\mathcal{B}_{\pm\mp\pm}$. Notice that these curves are now even closer to the boundaries of $W^u(p^\pm) \cap \Sigma$ and $W^s(p^\pm) \cap \Sigma$, respectively. Moreover, we find further intersection points between curves $\diamond_{\bar{z}}(\xi)$ and $\square_{\bar{z}}(\xi)$. For $0 < \xi < 1$ we find all expected four intersection points in the shown ξ-range; namely $(\xi, \bar{z}) \approx (0.4410, -0.7928)$, $(\xi, \bar{z}) \approx (0.4396, -0.5639)$, $(\xi, \bar{z}) \approx (0.4024, 0.7014)$ and $(\xi, \bar{z}) \approx (0.4740, 0.8367)$, which correspond to changes of overlap between the pairs $\mathcal{D}_{--\pm}$, $\mathcal{D}_{-+\pm}$, $\mathcal{D}_{+-\pm}$ and $\mathcal{D}_{++\pm}$, respectively. For $\xi > 1$,

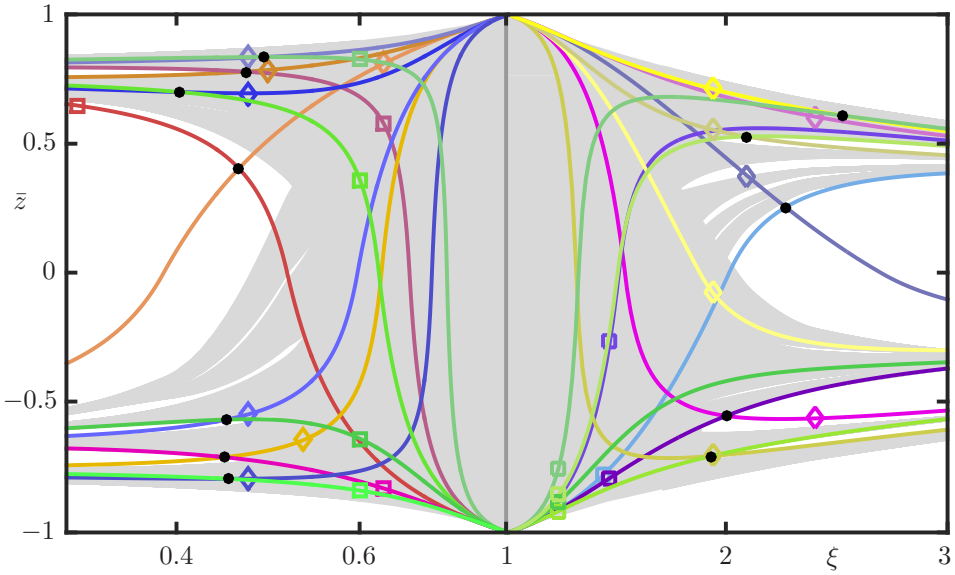

Figure 14: The curves $\diamond_{\bar{z}}(\xi)$ and $\square_{\bar{z}}(\xi)$ of opposing sub-boxes for $\mathcal{B}_{\pm}$ and $\mathcal{D}_{\pm}$, $\mathcal{D}_{\pm\mp}$ and $\mathcal{B}_{\pm\mp}$, and $\mathcal{B}_{\pm\mp\pm}$ and $\mathcal{D}_{\pm\mp\pm}$; shown with $W^u(p^{\pm}) \cap \Sigma$ and $W^s(p^{\pm}) \cap \Sigma$ as in Figs. 12 and 13.

on the other hand, Fig. 13 shows only the three intersection points $(\xi, \bar{z}) \approx (1.92181, -0.70477)$, $(\xi, \bar{z}) \approx (2.07822, 0.52975)$ and $(\xi, \bar{z}) \approx (2.51816, 0.61039)$; they correspond to changes in overlap between the pairs $\mathcal{B}_{--\pm}$, $\mathcal{B}_{+-\pm}$ and $\mathcal{B}_{++\pm}$, respectively. We did not find an intersection between the curves $\diamond_{\bar{z}}(\xi)$ for $\mathcal{B}_{-+-}$ and $\square_{\bar{z}}(\xi)$ for $\mathcal{B}_{-++}$ based on the data we computed for $\xi \in [1.01, 8.0]$. As was the case for $\mathcal{B}_{--}$ and $\mathcal{B}_{-+}$, this intersection point may well exist for values of ξ well beyond the ones considered here.

To summarise the discovered changes of overlap between successive sub-boxes, Fig. 14 shows only the relevant curves $\diamond_{\bar{z}}(\xi)$ and $\square_{\bar{z}}(\xi)$ for pairs of 'opposing boxes' that generate the intersection points we identified in Figs. 12 and 13. Notice how the respective intersection points are reasonably close to the disappearance of the biggest $\bar{z}$-gaps of $W^u(p^{\pm}) \cap \Sigma$ and $W^s(p^{\pm}) \cap \Sigma$, respectively. More specifically, the parts of the pairs of curves $\diamond_{\bar{z}}(\xi)$ and $\square_{\bar{z}}(\xi)$ corresponding to non-overlapping of the respective pairs of sub-boxes, as well as the intersection points themselves, actually lie in the respective gap. This reflects the fact that the boxes $\mathcal{B}$, $\mathcal{D}$ and their (pre)images provide an outer approximation of the local one-dimensional manifold of the hyperbolic set Λ. Hence, the ξ-values of the computed intersection points that represent a change in overlap, as well as those for further pairs of (pre)images of $\mathcal{B}$ and $\mathcal{D}$, provide an outer approximation of the ξ-interval around $\xi = 1$ where the carpet property holds and, hence, Λ is a blender.

5 Discussion and outlook

We have shown how to construct for the Hénon-like family H a parameter-dependent and tight linear box, a parallelepiped, whose forward images for $0 < \xi < 1$ and backward images for $\xi > 1$ intersect this box to yield a three-dimensional horseshoe that contains the local one-dimensional (un)stable manifold of the underlying hyperbolic set Λ. As we illustrated, sufficient overlap of the corresponding sequence of sub-boxes, when viewed along the relevant direction, is directly associated with Λ being a blender. As the contraction/expansion rate ξ is varied away from $\xi = 1$, gaps are created between these boxes, when viewed again along the relevant direction, and eventually Λ ceases to be a blender.

Due to the nonlinear nature of the map H, the (pre)images of the initial box deform in a non-affine way; here we identified two different yet related general phenomena. Firstly, while the

determining edges of all sub-boxes are aligned with the expanding direction, they are nevertheless curved and so are not parallel to the determining edges of the initial parallelepiped. Secondly, the successive sub-boxes are sheared increasingly. Both these effects are very relevant when one wants to decide whether there exists, or not, an overlap between sub-boxes when viewed from a given direction. In particular, the gaps between different pairs of sub-boxes in a chosen transverse section in a chosen direction do not all open up for the same value of ξ. Moreover, when such gaps open depends on the section and not just on the chosen direction. This represents a typical scenario, and it shows that the disappearance of the blender via the vertical separation of the two 'arms' of the three-dimensional horseshoe is a complicated and subtle process. While, as a first approximation, the affine construction provides a concise and persuasive explanation for the existence of blenders, it does not represent properly the details of their creation or disappearance.

Notwithstanding these issues, tracing the intersection points of the relevant determining edges of pairs of boxes with a transverse section provides an outer approximation of the ξ-range over which Λ should be expected to be a blender. Indeeed, we observed that the successive gaps of the respective one-dimensional manifolds appear at values of ξ that are necessarily closer to $\xi = 1$ but still quite near the ξ-values of the appearance of the gap between the corresponding boxes. This type of geometrical information should be useful also for subsequent investigations to determine an inner approximation of the ξ-range over which a blender exists. In particular, the presented box construction may inform and motivate a computer-assisted proof of the existence of a blender via rigorous computations based on interval arithmetic. This will require verifying that the (pre)image of the initial box satisfies topological as well as metric properties (expressed via cone conditions; see [6, 2]) required for a three-dimensional blender-horseshoe; this may be achieved in a rigorous way, for example, with the approach in [19, 18, 13]. In a similar spirit, it should be possible to provide a computer-assisted proof that Λ is not a blender when ξ is sufficiently far from $\xi = 1$.

In the intermediate range it is not so clear from a box construction whether a given hyperbolic set Λ is a blender or not. Namely, the mentioned distortion of iterates of the initial box, here under H or H^{-1}, is expected to play an important role. One observes an increasing nonlinear distortion at deeper levels of the three-dimensional horseshoe construction, which is mainly due to the difference between the expanding rates in the strong unstable and the center stable directions. This implies that a guess derived from the affine systems may not be suitable when attempting to prove that a hyperbolic set is a blender. The issue of distortion in the generic setting is known to experts in the field; in particular, dealing with it is an important part of the proof in [2] that a blender exists, and it is dexterously circumvented there by combining the observations of forward and backward iterations.

This effect of distortion is clearly pronounced near where the carpet property is lost. More precisely, both analytical as well as computer-assisted methods run into increasing diffuculties with obtaining the required estimates at deeper levels as the overlap between boxes decreases. This suggests that other approaches should be used when one is interested in how a blender can disappear or created as system parameters are changed. A specific example of an alternative approach is the computation of extremely long pieces of the respective one-dimensional manifolds. As we have shown in [11, 12] for the Hénon-like family H, computing $W^s(p^{\pm})$ or $W^u(p^{\pm})$, respectively, as arclength-parametrised curves allows one to provide convincing numerical evidence (albeit in a non-rigorous way) that any gaps in projection converge to zero with increasing arclength. This constitues a check that the carpet property is satisfied and, hence, Λ is a blender. Indeed, these one-dimensional manifolds exist for any value of $\xi > 1$ and of $0 < \xi < 1$, respectively, so that the break-up of the blender via the emergence of gaps in the projection can be studied. The details of this transition — the bifurcation of the blender — is the subject of ongoing research.

As a concluding remark, we hope that the work presented here will stimulate further investigations of blenders and their role for associated dynamics. As was already mentioned briefly in the introduction, there is a close connection between blenders and the C^1-robust existence of heterodimensional cycles [6, 2, 1, 4, 5, 3]. To convey the geometric idea, suppose that a diffeomorphism in $\mathbb{R}^3$ has a fixed or periodic point p with a one-dimensional stable manifold $W^s(p)$, which intersects the one-dimensional unstable manifold $W^u(q)$ of a second fixed or periodic point q of different index. Also, assume that the two-dimensional manifolds $W^u(p)$ and $W^s(q)$ intersect transversely so that there is a second connection and, hence, a heterodimensional cycle between p and q. While the second connection is robust, the first heteroclinic connection breaks when a C^1-perturbation is applied to the map. Suppose now that $p \in \Lambda$, where Λ is a blender and $W^u(q)$ approaches $W^s(\Lambda)$ along the direction associated with the carpet property. Then there exists a (different) heteroclinic connection for any sufficiently small C^1-perturbation of the map, meaning that the existence of the heteroclinic cycle is essentially a C^1-open property. In turn, it has been shown that the C^1-robust existence of heterodimensional cycles implies the existence of blenders; see [6, 2, 1, 4, 5, 3] for more details. While the Hénon family H is still the only explicit example of a diffeomorphism with a blender, one may attempt to find blenders in systems that feature heterodimensional cycles. A number of specific examples of such systems are known, including maps [9, 14] and vector fields [16, 20, 17], and the identification of a blender in any of them remains an interesting challenge.

References

[1] C. Bonatti, S. Crovisier, L. J. Díaz, and A. Wilkinson. What is... a blender? *Notices Amer. Math. Soc.*, 63(10):1175–1178, 2016.

[2] C. Bonatti and L. J. Díaz. Persistent nonhyperbolic transitive diffeomorphisms. *Ann. of Math. (2)*, 143(2):357–396, 1996.

[3] C. Bonatti and L. J. Díaz. Abundance of C^1-robust homoclinic tangencies. *Trans. Amer. Math. Soc.*, 364(10):5111–5148, 2012.

[4] C. Bonatti, L. J. Díaz, and S. Kiriki. Stabilization of heterodimensional cycles. *Nonlinearity*, 25(4):931–960, 2012.

[5] C. Bonatti, L. J. Díaz, and M. Viana. *Dynamics beyond Uniform Hyperbolicity. A global geometric and probabilistic perspective*, volume 102 of *Encyclopaedia Math. Sci.* Springer-Verlag, Berlin, 2005.

[6] L. J. Díaz, S. Kiriki, and K. Shinohara. Blenders in centre unstable Hénon-like families: with an application to heterodimensional bifurcations. *Nonlinearity*, 27(3):353–378, 2014.

[7] L. J. Díaz and S. A. Pérez. Blender-horseshoes in center-unstable Hénon-like families. In M. Pacifico and P. Guarino, editors, *New Trends in One-Dimensional Dynamics*, volume 285 of *Springer Proceedings in Mathematics and Statistics*, pages 137–163. Springer, New York, 2019.

[8] L. J. Díaz and S. A. Pérez. Hénon-like families and blender-horseshoes at nontransverse heterodimensional cycles. *International Journal of Bifurcation and Chaos*, 29(3):1930006, 2019.

[9] S. V. Gonchenko, I. I. Ovsyannikov, C. Simó, and D. Turaev. Three-dimensional Hénon-like maps and wild Lorenz-like attractors. *Internat. J. Bifur. Chaos Appl. Sci. Engrg.*, 15(11):3493–3508, 2005.

[10] M. Hénon. A two-dimensional mapping with a strange attractor. *Comm. Math. Phys.*, 50(1):69–77, 1976.

[11] S. Hittmeyer, B. Krauskopf, H. M. Osinga, and K. Shinohara. Existence of blenders in a Hénon-like family: geometric insights from invariant manifold computations. *Nonlinearity*, 31(10):R239–R267, 2018.

[12] S. Hittmeyer, B. Krauskopf, H. M. Osinga, and K. Shinohara. How to identify a hyperbolic set as a blender. *Discr. Cont. Dynam. Syst. – A*, 40(12):6815–6836, 2020.

[13] T. Kapela, M. Mrozek, D. Wilczak, and P. Zgliczyński. CAPD::DynSys: A flexible C++ toolbox for rigorous numerical analysis of dynamical systems. *Communications in Nonlinear Science and Numerical Simulation*, 101:105578, 2021.

[14] E. J. Kostelich, I. Kan, C. Grebogi, E. Ott, and J. A. Yorke. Unstable dimension variability: a source of nonhyperbolicity in chaotic systems. *Phys. D*, 109(1-2):81–90, 1997.

[15] B. Krauskopf and H. M. Osinga. Growing 1D and quasi-2D unstable manifolds of maps. *J. Comput. Phys.*, 146(1):404–419, 1998.

[16] D. Li. Homoclinic bifurcations that give rise to heterodimensional cycles near a saddle-focus equilibrium. *Nonlinearity*, 30(1):173–206, 2017.

[17] G. Mason, A. Hammerlindl, B. Krauskopf, and H. M. Osinga. Determining the global manifold structure of a continuous-time heterodimensional cycle. *J. Comput. Dynam.*, 9(3):393–419, 2022.

[18] P. Zgliczyński. Covering relations, cone conditions and the stable manifold theorem. *J. Differential Equations*, 246(5):1774–1819, 2009.

[19] P. Zgliczyński and M. Gidea. Covering relations for multidimensional dynamical systems. *J. Differential Equations*, 202(1):32–58, 2004.

[20] W. Zhang, B. Krauskopf, and V. Kirk. How to find a codimension-one heteroclinic cycle between two periodic orbits. *Discrete Contin. Dyn. Syst. Ser. A*, 32(8):2825–2851, 2012.